Measurement of the $t\bar{t}$ production cross section in 2 fb^{-1} of $p\bar{p}$ collisions at $\sqrt{s} = 1.96$ TeV using lepton plus jets events with soft muon b tagging

T. Aaltonen,[24] J. Adelman,[14] T. Akimoto,[56] B. Álvarez González,[12,t] S. Amerio,[44a,44b] D. Amidei,[35] A. Anastassov,[39] A. Annovi,[20] J. Antos,[15] G. Apollinari,[18] A. Apresyan,[49] T. Arisawa,[58] A. Artikov,[16] W. Ashmanskas,[18] A. Attal,[4] A. Aurisano,[54] F. Azfar,[43] P. Azzurri,[47a,47b] W. Badgett,[18] A. Barbaro-Galtieri,[29] V. E. Barnes,[49] B. A. Barnett,[26] V. Bartsch,[31] G. Bauer,[33] P.-H. Beauchemin,[34] F. Bedeschi,[47a] D. Beecher,[31] S. Behari,[26] G. Bellettini,[47a,47b] J. Bellinger,[60] D. Benjamin,[17] A. Beretvas,[18] J. Beringer,[29] A. Bhatti,[51] M. Binkley,[18] D. Bisello,[44a,44b] I. Bizjak,[31,y] R. E. Blair,[2] C. Blocker,[7] B. Blumenfeld,[26] A. Bocci,[17] A. Bodek,[50] V. Boisvert,[50] G. Bolla,[49] D. Bortoletto,[49] J. Boudreau,[48] A. Boveia,[11] B. Brau,[11,b] A. Bridgeman,[25] L. Brigliadori,[44a] C. Bromberg,[36] E. Brubaker,[14] J. Budagov,[16] H. S. Budd,[50] S. Budd,[25] S. Burke,[18] K. Burkett,[18] G. Busetto,[44a,44b] P. Bussey,[22] A. Buzatu,[34] K. L. Byrum,[2] S. Cabrera,[17,v] C. Calancha,[32] M. Campanelli,[36] M. Campbell,[35] F. Canelli,[14,18] A. Canepa,[46] B. Carls,[25] D. Carlsmith,[60] R. Carosi,[47a] S. Carrillo,[19,o] S. Carron,[34] B. Casal,[12] M. Casarsa,[18] A. Castro,[6a,6b] P. Catastini,[47a,47c] D. Cauz,[55a,55b] V. Cavaliere,[47a,47c] M. Cavalli-Sforza,[4] A. Cerri,[29] L. Cerrito,[31,p] S. H. Chang,[28] Y. C. Chen,[1] M. Chertok,[8] G. Chiarelli,[47a] G. Chlachidze,[18] F. Chlebana,[18] K. Cho,[28] D. Chokheli,[16] J. P. Chou,[23] G. Choudalakis,[33] S. H. Chuang,[53] K. Chung,[13] W. H. Chung,[60] Y. S. Chung,[50] T. Chwalek,[27] C. I. Ciobanu,[45] M. A. Ciocci,[47a,47c] A. Clark,[21] D. Clark,[7] G. Compostella,[44a] M. E. Convery,[18] J. Conway,[8] M. Cordelli,[20] G. Cortiana,[44a,44b] C. A. Cox,[8] D. J. Cox,[8] F. Crescioli,[47a,47b] C. Cuenca Almenar,[8,v] J. Cuevas,[12,t] R. Culbertson,[18] J. C. Cully,[35] D. Dagenhart,[18] M. Datta,[18] T. Davies,[22] P. de Barbaro,[50] S. De Cecco,[52a] A. Deisher,[29] G. De Lorenzo,[4] M. Dell'Orso,[47a,47b] C. Deluca,[4] L. Demortier,[51] J. Deng,[17] M. Deninno,[6a] P. F. Derwent,[18] G. P. di Giovanni,[45] C. Dionisi,[52a,52b] B. Di Ruzza,[55a,55b] J. R. Dittmann,[5] M. D'Onofrio,[4] S. Donati,[47a,47b] P. Dong,[9] J. Donini,[44a] T. Dorigo,[44a] S. Dube,[53] J. Efron,[40] A. Elagin,[54] R. Erbacher,[8] D. Errede,[25] S. Errede,[25] R. Eusebi,[18] H. C. Fang,[29] S. Farrington,[43] W. T. Fedorko,[14] R. G. Feild,[61] M. Feindt,[27] J. P. Fernandez,[32] C. Ferrazza,[47a,47d] R. Field,[19] G. Flanagan,[49] R. Forrest,[8] M. J. Frank,[5] M. Franklin,[23] J. C. Freeman,[18] I. Furic,[19] M. Gallinaro,[52a] J. Galyardt,[13] F. Garberson,[11] J. E. Garcia,[21] A. F. Garfinkel,[49] K. Genser,[18] H. Gerberich,[25] D. Gerdes,[35] A. Gessler,[27] S. Giagu,[52a,52b] V. Giakoumopoulou,[3] P. Giannetti,[47a] K. Gibson,[48] J. L. Gimmell,[50] C. M. Ginsburg,[18] N. Giokaris,[3] M. Giordani,[55a,55b] P. Giromini,[20] M. Giunta,[47a,47b] G. Giurgiu,[26] V. Glagolev,[16] D. Glenzinski,[18] M. Gold,[38] N. Goldschmidt,[19] A. Golossanov,[18] G. Gomez,[12] G. Gomez-Ceballos,[33] M. Goncharov,[33] O. González,[32] I. Gorelov,[38] A. T. Goshaw,[17] K. Goulianos,[51] A. Gresele,[44a,44b] S. Grinstein,[23] C. Grosso-Pilcher,[14] R. C. Group,[18] U. Grundler,[25] J. Guimaraes da Costa,[23] Z. Gunay-Unalan,[36] C. Haber,[29] K. Hahn,[33] S. R. Hahn,[18] E. Halkiadakis,[53] B.-Y. Han,[50] J. Y. Han,[50] F. Happacher,[20] K. Hara,[56] D. Hare,[53] M. Hare,[57] S. Harper,[43] R. F. Harr,[59] R. M. Harris,[18] M. Hartz,[48] K. Hatakeyama,[51] C. Hays,[43] M. Heck,[27] A. Heijboer,[46] J. Heinrich,[46] C. Henderson,[33] M. Herndon,[60] J. Heuser,[27] S. Hewamanage,[5] D. Hidas,[17] C. S. Hill,[11,d] D. Hirschbuehl,[27] A. Hocker,[18] S. Hou,[1] M. Houlden,[30] S.-C. Hsu,[29] B. T. Huffman,[43] R. E. Hughes,[40] U. Husemann,[61] M. Hussein,[36] J. Huston,[36] J. Incandela,[11] G. Introzzi,[47a] M. Iori,[52a,52b] A. Ivanov,[8] E. James,[18] D. Jang,[13] B. Jayatilaka,[17] E. J. Jeon,[28] M. K. Jha,[6a] S. Jindariani,[18] W. Johnson,[8] M. Jones,[49] K. K. Joo,[28] S. Y. Jun,[13] J. E. Jung,[28] T. R. Junk,[18] T. Kamon,[54] D. Kar,[19] P. E. Karchin,[59] Y. Kato,[42,m] R. Kephart,[18] J. Keung,[46] V. Khotilovich,[54] B. Kilminster,[18] D. H. Kim,[28] H. S. Kim,[28] H. W. Kim,[28] J. E. Kim,[28] M. J. Kim,[20] S. B. Kim,[28] S. H. Kim,[56] Y. K. Kim,[14] N. Kimura,[56] L. Kirsch,[7] S. Klimenko,[19] B. Knuteson,[33] B. R. Ko,[17] K. Kondo,[58] D. J. Kong,[28] J. Konigsberg,[19] A. Korytov,[19] A. V. Kotwal,[17] M. Kreps,[27] J. Kroll,[46] D. Krop,[14] N. Krumnack,[5] M. Kruse,[17] V. Krutelyov,[11] T. Kubo,[56] T. Kuhr,[27] N. P. Kulkarni,[59] M. Kurata,[56] S. Kwang,[14] A. T. Laasanen,[49] S. Lami,[47a] S. Lammel,[18] M. Lancaster,[31] R. L. Lander,[8] K. Lannon,[40,s] A. Lath,[53] G. Latino,[47a,47c] I. Lazzizzera,[44a,44b] T. LeCompte,[2] E. Lee,[54] H. S. Lee,[14] S. W. Lee,[54,u] S. Leone,[47a] J. D. Lewis,[18] C.-S. Lin,[29] J. Linacre,[43] M. Lindgren,[18] E. Lipeles,[46] T. M. Liss,[25] A. Lister,[8] D. O. Litvintsev,[18] C. Liu,[48] T. Liu,[18] N. S. Lockyer,[46] A. Loginov,[61] M. Loreti,[44a,44b] L. Lovas,[15] D. Lucchesi,[44a,44b] C. Luci,[52a,52b] J. Lueck,[27] P. Lujan,[29] P. Lukens,[18] G. Lungu,[51] L. Lyons,[43] J. Lys,[29] R. Lysak,[15] D. MacQueen,[34] R. Madrak,[18] K. Maeshima,[18] K. Makhoul,[33] T. Maki,[24] P. Maksimovic,[26] S. Malde,[43] S. Malik,[31] G. Manca,[30,f] A. Manousakis-Katsikakis,[3] F. Margaroli,[49] C. Marino,[27] C. P. Marino,[25] A. Martin,[61] V. Martin,[22,l] M. Martínez,[4] R. Martínez-Ballarín,[32] T. Maruyama,[56] P. Mastrandrea,[52a] T. Masubuchi,[56] M. Mathis,[26] M. E. Mattson,[59] P. Mazzanti,[6a] K. S. McFarland,[50] P. McIntyre,[54] R. McNulty,[30,k] A. Mehta,[30] P. Mehtala,[24] A. Menzione,[47a] P. Merkel,[49] C. Mesropian,[51] T. Miao,[18] N. Miladinovic,[7] R. Miller,[36] C. Mills,[23] M. Milnik,[27] A. Mitra,[1] G. Mitselmakher,[19] H. Miyake,[56] N. Moggi,[6a] C. S. Moon,[28] R. Moore,[18] M. J. Morello,[47a,47b] J. Morlock,[27] P. Movilla Fernandez,[18] J. Mülmenstädt,[29] A. Mukherjee,[18] Th. Muller,[27] R. Mumford,[26] P. Murat,[18] M. Mussini,[6a,6b] J. Nachtman,[18] Y. Nagai,[56] A. Nagano,[56] J. Naganoma,[56] K. Nakamura,[56] I. Nakano,[41] A. Napier,[57] V. Necula,[17] J. Nett,[60] C. Neu,[46,w]

M. S. Neubauer,[25] S. Neubauer,[27] J. Nielsen,[29,h] L. Nodulman,[2] M. Norman,[10] O. Norniella,[25] E. Nurse,[31] L. Oakes,[43] S. H. Oh,[17] Y. D. Oh,[28] I. Oksuzian,[19] T. Okusawa,[42] R. Orava,[24] K. Osterberg,[24] S. Pagan Griso,[44a,44b] E. Palencia,[18] V. Papadimitriou,[18] A. Papaikonomou,[27] A. A. Paramonov,[14] B. Parks,[40] S. Pashapour,[34] J. Patrick,[18] G. Pauletta,[55a,55b] M. Paulini,[13] C. Paus,[33] T. Peiffer,[27] D. E. Pellett,[8] A. Penzo,[55a] T. J. Phillips,[17] G. Piacentino,[47a] E. Pianori,[46] L. Pinera,[19] K. Pitts,[25] C. Plager,[9] L. Pondrom,[60] O. Poukhov,[16,a] N. Pounder,[43] F. Prakoshyn,[16] A. Pronko,[18] J. Proudfoot,[2] F. Ptohos,[18,j] E. Pueschel,[13] G. Punzi,[47a,47b] J. Pursley,[60] J. Rademacker,[43,d] A. Rahaman,[48] V. Ramakrishnan,[60] N. Ranjan,[49] I. Redondo,[32] P. Renton,[43] M. Renz,[27] M. Rescigno,[52a] S. Richter,[27] F. Rimondi,[6a,6b] L. Ristori,[47a] A. Robson,[22] T. Rodrigo,[12] T. Rodriguez,[46] E. Rogers,[25] S. Rolli,[57] R. Roser,[18] M. Rossi,[55a] R. Rossin,[11] P. Roy,[34] A. Ruiz,[12] J. Russ,[13] V. Rusu,[18] B. Rutherford,[18] H. Saarikko,[24] A. Safonov,[54] W. K. Sakumoto,[50] O. Saltó,[4] L. Santi,[55a,55b] S. Sarkar,[52a,52b] L. Sartori,[47a] K. Sato,[18] A. Savoy-Navarro,[45] P. Schlabach,[18] A. Schmidt,[27] E. E. Schmidt,[18] M. A. Schmidt,[14] M. P. Schmidt,[61,a] M. Schmitt,[39] T. Schwarz,[8] L. Scodellaro,[12] A. Scribano,[47a,47c] F. Scuri,[47a] A. Sedov,[49] S. Seidel,[38] Y. Seiya,[42] A. Semenov,[16] L. Sexton-Kennedy,[18] F. Sforza,[47a] A. Sfyrla,[25] S. Z. Shalhout,[59] T. Shears,[30] P. F. Shepard,[48] M. Shimojima,[56,r] S. Shiraishi,[14] M. Shochet,[14] Y. Shon,[60] I. Shreyber,[37] A. Sidoti,[47a] P. Sinervo,[34] A. Sisakyan,[16] A. J. Slaughter,[18] J. Slaunwhite,[40] K. Sliwa,[57] J. R. Smith,[8] F. D. Snider,[18] R. Snihur,[34] A. Soha,[8] S. Somalwar,[53] V. Sorin,[36] J. Spalding,[18] T. Spreitzer,[34] P. Squillacioti,[47a,47b] M. Stanitzki,[61] R. St. Denis,[22] B. Stelzer,[34] O. Stelzer-Chilton,[34] D. Stentz,[39] J. Strologas,[38] G. L. Strycker,[35] D. Stuart,[11] J. S. Suh,[28] A. Sukhanov,[19] I. Suslov,[16] T. Suzuki,[56] A. Taffard,[25,g] R. Takashima,[41] Y. Takeuchi,[56] R. Tanaka,[41] M. Tecchio,[35] P. K. Teng,[1] K. Terashi,[51] J. Thom,[18,i] A. S. Thompson,[22] G. A. Thompson,[25] E. Thomson,[46] P. Tipton,[61] P. Ttito-Guzmán,[32] S. Tkaczyk,[18] D. Toback,[54] S. Tokar,[15] K. Tollefson,[36] T. Tomura,[56] D. Tonelli,[18] S. Torre,[20] D. Torretta,[18] P. Totaro,[55a,55b] S. Tourneur,[45] M. Trovato,[47a] S.-Y. Tsai,[1] Y. Tu,[46] N. Turini,[47a,47c] F. Ukegawa,[56] S. Vallecorsa,[21] N. van Remortel,[24,c] A. Varganov,[35] E. Vataga,[47a,47d] F. Vázquez,[19,o] G. Velev,[18] C. Vellidis,[3] M. Vidal,[32] R. Vidal,[18] I. Vila,[12] R. Vilar,[12] T. Vine,[31] M. Vogel,[38] I. Volobouev,[29,u] G. Volpi,[47a,47b] P. Wagner,[46] R. G. Wagner,[2] R. L. Wagner,[18] W. Wagner,[27,x] J. Wagner-Kuhr,[27] T. Wakisaka,[42] R. Wallny,[9] S. M. Wang,[1] A. Warburton,[34] D. Waters,[31] M. Weinberger,[54] J. Weinelt,[27] W. C. Wester III,[18] B. Whitehouse,[57] D. Whiteson,[46,g] A. B. Wicklund,[2] E. Wicklund,[18] S. Wilbur,[14] G. Williams,[34] H. H. Williams,[46] P. Wilson,[18] B. L. Winer,[40] P. Wittich,[18,i] S. Wolbers,[18] C. Wolfe,[14] T. Wright,[35] X. Wu,[21] F. Würthwein,[10] S. Xie,[33] A. Yagil,[10] K. Yamamoto,[42] J. Yamaoka,[17] U. K. Yang,[14,q] Y. C. Yang,[28] W. M. Yao,[29] G. P. Yeh,[18] J. Yoh,[18] K. Yorita,[58] T. Yoshida,[42,n] G. B. Yu,[50] I. Yu,[28] S. S. Yu,[18] J. C. Yun,[18] L. Zanello,[52a,52b] A. Zanetti,[55a] X. Zhang,[25] Y. Zheng,[9,e] and S. Zucchelli[6a,6b]

(CDF Collaboration)

[1]*Institute of Physics, Academia Sinica, Taipei, Taiwan 11529, Republic of China*
[2]*Argonne National Laboratory, Argonne, Illinois 60439, USA*
[3]*University of Athens, 157 71 Athens, Greece*
[4]*Institut de Fisica d'Altes Energies, Universitat Autonoma de Barcelona, E-08193, Bellaterra (Barcelona), Spain*
[5]*Baylor University, Waco, Texas 76798, USA*
[6a]*Istituto Nazionale di Fisica Nucleare Bologna, I-40127 Bologna, Italy*
[6b]*University of Bologna, I-40127 Bologna, Italy*
[7]*Brandeis University, Waltham, Massachusetts 02254, USA*
[8]*University of California, Davis, Davis, California 95616, USA*
[9]*University of California, Los Angeles, Los Angeles, California 90024, USA*
[10]*University of California, San Diego, La Jolla, California 92093, USA*
[11]*University of California, Santa Barbara, Santa Barbara, California 93106, USA*
[12]*Instituto de Fisica de Cantabria, CSIC-University of Cantabria, 39005 Santander, Spain*
[13]*Carnegie Mellon University, Pittsburgh, Pennsylvania 15213, USA*
[14]*Enrico Fermi Institute, University of Chicago, Chicago, Illinois 60637, USA*
[15]*Comenius University, 842 48 Bratislava, Slovakia;*
Institute of Experimental Physics, 040 01 Kosice, Slovakia
[16]*Joint Institute for Nuclear Research, RU-141980 Dubna, Russia*
[17]*Duke University, Durham, North Carolina 27708, USA*
[18]*Fermi National Accelerator Laboratory, Batavia, Illinois 60510, USA*
[19]*University of Florida, Gainesville, Florida 32611, USA*
[20]*Laboratori Nazionali di Frascati, Istituto Nazionale di Fisica Nucleare, I-00044 Frascati, Italy*
[21]*University of Geneva, CH-1211 Geneva 4, Switzerland*
[22]*Glasgow University, Glasgow G12 8QQ, United Kingdom*

[23]*Harvard University, Cambridge, Massachusetts 02138, USA*
[24]*Division of High Energy Physics, Department of Physics, University of Helsinki and Helsinki Institute of Physics, FIN-00014, Helsinki, Finland*
[25]*University of Illinois, Urbana, Illinois 61801, USA*
[26]*The Johns Hopkins University, Baltimore, Maryland 21218, USA*
[27]*Institut für Experimentelle Kernphysik, Universität Karlsruhe, 76128 Karlsruhe, Germany*
[28]*Center for High Energy Physics: Kyungpook National University, Daegu 702-701, Korea; Seoul National University, Seoul 151-742, Korea; Sungkyunkwan University, Suwon 440-746, Korea; Korea Institute of Science and Technology Information, Daejeon, 305-806, Korea; Chonnam National University, Gwangju, 500-757, Korea*
[29]*Ernest Orlando Lawrence Berkeley National Laboratory, Berkeley, California 94720, USA*
[30]*University of Liverpool, Liverpool L69 7ZE, United Kingdom*
[31]*University College London, London WC1E 6BT, United Kingdom*
[32]*Centro de Investigaciones Energeticas Medioambientales y Tecnologicas, E-28040 Madrid, Spain*
[33]*Massachusetts Institute of Technology, Cambridge, Massachusetts 02139, USA*
[34]*Institute of Particle Physics: McGill University, Montréal, Québec, Canada H3A 2T8; Simon Fraser University, Burnaby, British Columbia, Canada V5A 1S6; University of Toronto, Toronto, Ontario, Canada M5S 1A7; and TRIUMF, Vancouver, British Columbia, Canada V6T 2A3*
[35]*University of Michigan, Ann Arbor, Michigan 48109, USA*
[36]*Michigan State University, East Lansing, Michigan 48824, USA*
[37]*Institution for Theoretical and Experimental Physics, ITEP, Moscow 117259, Russia*
[38]*University of New Mexico, Albuquerque, New Mexico 87131, USA*
[39]*Northwestern University, Evanston, Illinois 60208, USA*
[40]*The Ohio State University, Columbus, Ohio 43210, USA*
[41]*Okayama University, Okayama 700-8530, Japan*
[42]*Osaka City University, Osaka 588, Japan*
[43]*University of Oxford, Oxford OX1 3RH, United Kingdom*
[44a]*Istituto Nazionale di Fisica Nucleare, Sezione di Padova-Trento, I-35131 Padova, Italy*
[44b]*University of Padova, I-35131 Padova, Italy*
[45]*LPNHE, Universite Pierre et Marie Curie/IN2P3-CNRS, UMR7585, Paris, F-75252 France*
[46]*University of Pennsylvania, Philadelphia, Pennsylvania 19104, USA*
[47a]*Istituto Nazionale di Fisica Nucleare Pisa, I-56127 Pisa, Italy*
[47b]*University of Pisa, I-56127 Pisa, Italy*
[47c]*University of Siena, I-56127 Pisa, Italy*

[a]Deceased.
[b]Visitor from University of Massachusetts Amherst, Amherst, MA 01003, USA.
[c]Visitor from Universiteit Antwerpen, B-2610 Antwerp, Belgium.
[d]Visitor from University of Bristol, Bristol BS8 1TL, United Kingdom.
[e]Visitor from Chinese Academy of Sciences, Beijing 100864, China.
[f]Visitor from Istituto Nazionale di Fisica Nucleare, Sezione di Cagliari, 09042 Monserrato (Cagliari), Italy.
[g]Visitor from University of California Irvine, Irvine, CA 92697, USA.
[h]Visitor from University of California Santa Cruz, Santa Cruz, CA 95064, USA.
[i]Visitor from Cornell University, Ithaca, NY 14853, USA.
[j]Visitor from University of Cyprus, Nicosia CY-1678, Cyprus.
[k]Visitor from University College Dublin, Dublin 4, Ireland.
[l]Visitor from University of Edinburgh, Edinburgh EH9 3JZ, United Kingdom.
[m]Visitor from University of Fukui, Fukui City, Fukui Prefecture, Japan 910-0017.
[n]Visitor from Kinki University, Higashi-Osaka City, Japan 577-8502.
[o]Visitor from Universidad Iberoamericana, Mexico D.F., Mexico.
[p]Visitor from Queen Mary, University of London, London, E1 4NS, United Kingdom.
[q]Visitor from University of Manchester, Manchester M13 9PL, United Kingdom.
[r]Visitor from Nagasaki Institute of Applied Science, Nagasaki, Japan.
[s]Visitor from University of Notre Dame, Notre Dame, IN 46556, USA.
[t]Visitor from University de Oviedo, E-33007 Oviedo, Spain.
[u]Visitor from Texas Tech University, Lubbock, TX 79609, USA.
[v]Visitor from IFIC (CSIC-Universitat de Valencia), 46071 Valencia, Spain.
[w]Visitor from University of Virginia, Charlottesville, VA 22904, USA.
[x]Visitor from Bergische Universität Wuppertal, 42097 Wuppertal, Germany.
[y]On leave from J. Stefan Institute, Ljubljana, Slovenia.

[47d]*Scuola Normale Superiore, I-56127 Pisa, Italy*
[48]*University of Pittsburgh, Pittsburgh, Pennsylvania 15260, USA*
[49]*Purdue University, West Lafayette, Indiana 47907, USA*
[50]*University of Rochester, Rochester, New York 14627, USA*
[51]*The Rockefeller University, New York, New York 10021, USA*
[52a]*Istituto Nazionale di Fisica Nucleare, Sezione di Roma 1, I-00185 Roma, Italy*
[52b]*Sapienza Università di Roma, I-00185 Roma, Italy*
[53]*Rutgers University, Piscataway, New Jersey 08855, USA*
[54]*Texas A&M University, College Station, Texas 77843, USA*
[55a]*Istituto Nazionale di Fisica Nucleare Trieste/Udine, I-34100 Trieste, Italy*
[55b]*University of Trieste/Udine, I-33100 Udine, Italy*
[56]*University of Tsukuba, Tsukuba, Ibaraki 305, Japan*
[57]*Tufts University, Medford, Massachusetts 02155, USA*
[58]*Waseda University, Tokyo 169, Japan*
[59]*Wayne State University, Detroit, Michigan 48201, USA*
[60]*University of Wisconsin, Madison, Wisconsin 53706, USA*
[61]*Yale University, New Haven, Connecticut 06520, USA*
(Received 26 January 2009; published 20 March 2009)

We present a measurement of the $t\bar{t}$ production cross section in $p\bar{p}$ collisions at $\sqrt{s} = 1.96$ TeV using events containing a high transverse momentum electron or muon, three or more jets, and missing transverse energy. Events consistent with $t\bar{t}$ decay are found by identifying jets containing candidate heavy-flavor semileptonic decays to muons. The measurement uses a CDF run II data sample corresponding to 2 fb^{-1} of integrated luminosity. Based on 248 candidate events with three or more jets and an expected background of 79.5 ± 5.3 events, we measure a production cross section of 9.1 ± 1.6 pb.

DOI: 10.1103/PhysRevD.79.052007 PACS numbers: 13.85.Ni, 13.85.Qk, 14.65.Ha

I. INTRODUCTION

Top quark pair production in hadronic collisions in the standard model (SM) proceeds via either quark-antiquark annihilation or through gluon-gluon fusion. At the Fermilab Tevatron collider, with a center-of-mass energy of 1.96 TeV, the production is expected to be dominated by quark-antiquark annihilation. For a top mass of 175 GeV/c^2 the theoretical cross section is calculated to be 6.6 ± 0.6 pb [1] and decreases by approximately 0.2 pb for each 1 GeV/c^2 increase in the top mass over the range $170\ \text{GeV}/c^2 < M_{\text{top}} < 190\ \text{GeV}/c^2$.

Measurements of the cross section for top quark pair production provide a test of the expected QCD production mechanism as well as of the standard model decay into a W boson and a bottom quark, $t \rightarrow Wb$. Nonstandard model production mechanisms could enhance the measured cross section, and nonstandard model decays could suppress the measured value, which assumes a branching fraction of $t \rightarrow Wb$ of 100%.

In this paper we describe a measurement of the $t\bar{t}$ production cross section in $p\bar{p}$ collisions at $\sqrt{s} = 1.96$ TeV with the CDF II detector at the Fermilab Tevatron. The measurement assumes the standard model decay $t \rightarrow Wb$ of the top quark, providing a final state from $t\bar{t}$ production that includes two W bosons and two bottom quarks. We select events where one of the W bosons decays to an electron or muon which has large momentum transverse to the beam direction (P_T) plus a neutrino. The neutrino is undetected and results in an imbalance in transverse momentum. This imbalance is labeled ''missing E_T'' ($\not\!\!E_T$) because it is reconstructed based on the flow of energy in the calorimeter [2]. The other W boson in the event decays hadronically to a pair of quarks. The two quarks from the W boson and the two b quarks from the top decays hadronize and are observed as jets of charged and neutral particles. We take advantage of the semileptonic decay of b-hadrons to muons to identify final-state jets that result from hadronization of the bottom quarks expected in the top decay. This ''soft-lepton tagging'' with muons, or SLTμ, is effective in reducing the background to the $t\bar{t}$ signal from W plus multijet production. This technique is complementary to measurements that take advantage of the long lifetime of b-hadrons to identify jets from bottom quark hadronization through the presence of a decay vertex displaced from the primary interaction [3].

This measurement is an update of the measurement described in [4], which was made with approximately one-tenth of the integrated luminosity used here. Full details of this analysis are presented in [5]. In addition to the larger data set, we report here on a new method for evaluating the background from ''mistags,'' i.e., those SLTμs that do not arise from semileptonic decays of heavy-flavor (HF) quarks. This is described in Sec. VI.

II. THE CDF DETECTOR

The CDF II detector is described in detail in [6]. We describe briefly those elements of the detector that are central to this analysis. CDF II is a nearly azimuthally

and forward-backward symmetric detector designed to study $p\bar{p}$ interactions at the Fermilab Tevatron. It consists of a magnetic spectrometer surrounded by calorimeters and muon chambers. An elevation view of the CDF II detector is shown in Fig. 1.

Charged particles are tracked inside a 1.4 T solenoidal magnetic field by an 8-layer silicon strip detector, covering radii from 1.5 to 28 cm, followed by the central outer tracker (COT), an open-cell drift chamber that provides up to 96 measurements of charged-particle position over the radial region from 40 to 137 cm. The 96 COT measurements are arranged in 8 ''superlayers'' of 12 sense wires each that alternate between axial and 2° stereo orientations. The silicon detector tracks charged particles with high efficiency for $|\eta| < 2.0$, and the COT for $|\eta| < 1.0$ [2].

Surrounding the tracking system, and outside the magnet coil, are the electromagnetic and hadronic calorimeters, used to measure charged and neutral particle energies. The electromagnetic calorimeter is a lead-scintillator sandwich and the hadronic calorimeter is an iron-scintillator sandwich. Both calorimeters are segmented in azimuth and polar angle to provide directional information for the energy deposition. The segmentation varies with position on the detector and is 15° in azimuth by 0.1 units of η in the central region ($|\eta| < 1.1$). Segmentation in the plug region ($1.1 < |\eta| < 3.6$) is 7.5° ($|\eta| < 2.1$) or 15° ($|\eta| > 2.1$) in azimuth and ranges from 0.1 to 0.64 units of η (corresponding to a nearly constant 2.7° change in polar angle). The electromagnetic calorimeters are instrumented with proportional and scintillating strip detectors that measure the transverse profile of electromagnetic showers at a depth corresponding to the shower maximum.

Behind the central calorimeter are four layers of central muon drift chambers (CMU) covering $|\eta| < 0.6$. The calorimeter provides approximately 1 m of steel shielding. Behind an additional 60 cm of steel in the central region sit an additional four layers of muon drift chambers (CMP) arranged in a box-shaped layout around the central detector. Central muon extension (CMX) chambers, which are arrayed in a conical geometry, provide muon detection for the region $0.6 < |\eta| < 1.0$ with between four and six layers of drift chamber, depending on zenith angle. The CMX chambers covering from 225° to 315° in azimuth are known as the ''miniskirt'' while those covering from 75° to 105° in azimuth are known as the ''keystone.'' The remainder of the CMX chambers are referred to as the ''arches.'' The muon chambers measure the coordinate of hits in the drift direction, x, via a drift time measurement and a calibrated drift velocity, and for CMU and CMX, the longitudinal coordinate, z. The longitudinal coordinate is measured in CMU by comparing the pulse heights, encoded in time over threshold, of pulses at opposite ends of the sense wire. In CMX, the conical geometry provides a small stereo angle from which the z coordinate of track segments can be measured. Reconstructed track segments in CMU and CMP have a maximum of 4 hits, and in CMX a maximum of 6 hits.

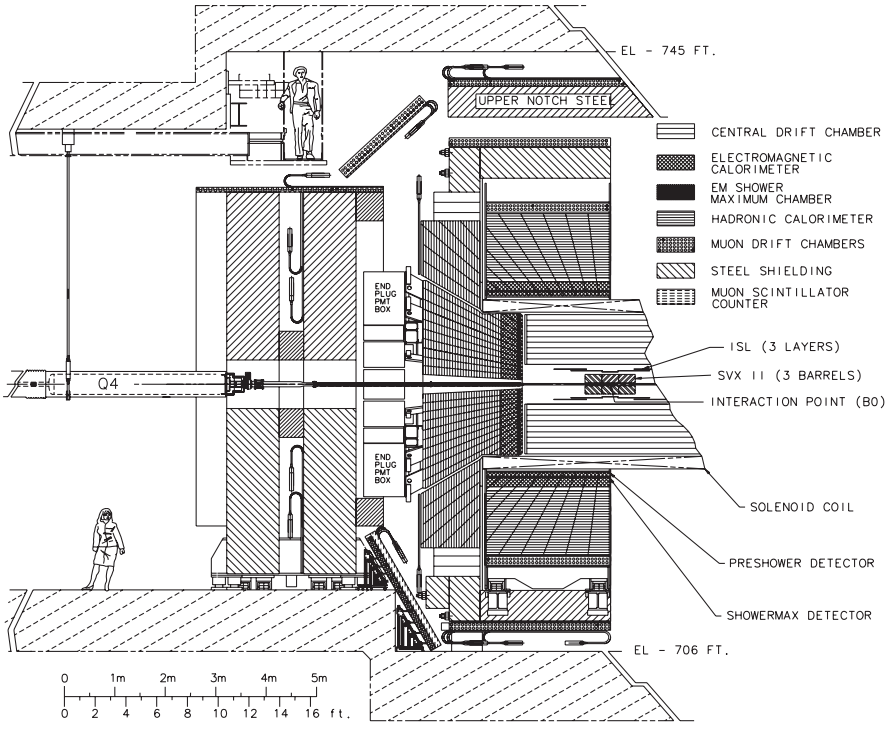

FIG. 1. Elevation view of the CDF II detector.

III. DATA SAMPLE AND EVENT SELECTION

This analysis is based on an integrated luminosity of 2034 ± 120 pb^{-1} [7] (1993 pb^{-1} with the CMX detector operational) collected with the CDF II detector between March 2002 and May 2007.

A. Kinematic selection

The triggering and off-line event selection used in this analysis are nearly identical to that used in the previous analysis described in [4]. For completeness we reproduce the basic trigger and selection criteria here and highlight the few differences.

CDF II employs a three level trigger system, the first two consisting of special purpose hardware and the third consisting of a farm of commodity computers. Triggers for this analysis are based on selecting high transverse momentum electrons and muons. The electron sample is triggered as follows: At the first trigger level, events are selected by requiring a track with $P_T > 8$ GeV/c matched to an electromagnetic calorimeter tower with $E_T > 8$ GeV and little energy in the hadronic calorimeter behind it. At the second trigger level, calorimeter energy clusters are assembled, and the track found at the first level must be matched to an electromagnetic cluster with $E_T > 16$ GeV. At the third level, off-line reconstruction is performed and an electron candidate with $E_T > 18$ GeV is required. The muon sample trigger begins at the first trigger level with a track with $P_T > 4$ GeV/c matched to hits in the CMU and CMP chambers or a track with $P_T > 8$ GeV/c matched to hits in the CMX chambers. At the second level a track with $P_T > 8$ GeV/c is required in the event for all but the first few percent of the integrated luminosity, for which triggers at the first level were fed directly to the third level trigger. At the third trigger level a reconstructed track with $P_T > 18$ GeV/c is required to be matched to the muon chamber hits.

From the inclusive lepton data set produced by the electron and muon triggers described above, we select off line an inclusive W plus jets candidate sample by requiring a reconstructed isolated electron with $E_T > 20$ GeV or muon with $P_T > 20$ GeV/c, $\not\!\!E_T > 30$ GeV and at least 1 jet with $E_T > 20$ GeV and $|\eta| < 2.0$. We define an isolation parameter, I, as the calorimeter energy in a cone of $\Delta R \equiv \sqrt{\Delta\eta^2 + \Delta\phi^2} < 0.4$ around the lepton (not including the lepton energy itself) divided by the E_T (P_T) of the lepton. We select isolated electrons (muons) by requiring $I < 0.1$. Electrons and muons satisfying these criteria are called the "primary lepton." Jets are identified using a fixed-cone algorithm with a cone size of $\Delta R = 0.4$ and are constrained to originate at the $p\bar{p}$ collision vertex. Their energies are corrected to account for detector response variations in η, drifts in calorimeter gain, nonlinearity of calorimeter energy response, multiple interactions in an event, and for energy loss in uninstrumented regions of the detector. These corrections bring the jet energies, on average, back to the sum P_T of the particles in the jet cone, but not all the way back to the parton energy. This is slightly different from the previous analysis [4] where the correction was done only for response variations in η, gain drifts, and multiple interactions. The jet counting threshold in that analysis was $E_T > 15$ GeV, which corresponds roughly to the $E_T > 20$ GeV used here with the additional corrections. The missing transverse energy is corrected to account for the shifts in jet energies due to the jet corrections above, and the $\not\!\!E_T$ threshold has been raised from 20 GeV in the previous analysis to 30 GeV here, consistent with the change in jet corrections. Z boson candidate events are rejected by removing events in which a second, same flavor, opposite sign isolated lepton, together with the primary lepton, makes an invariant mass between 76 and 106 GeV/c^2. The acceptance of these selection criteria for $t\bar{t}$ events is discussed in Sec. V.

The $t\bar{t}$ signal region consists of W candidate events with 3 or more jets, while the $W + 1$ and $W + 2$ jet events provide a control sample with little signal contamination.

The data set selected above is dominated by QCD production of W bosons with multiple jets. As a first stage of background reduction, we define a total event transverse energy, H_T, as the scalar sum of the electron E_T or muon P_T, $\not\!\!E_T$ and jet E_T for jets with $E_T > 8$ GeV and $|\eta| < 2.4$. Figure 2 shows a comparison between the H_T distributions for simulated $t\bar{t}$ and W + jets events with at least 3 jets. For 3 or more jet events, we require $H_T > 200$ GeV. This requirement rejects approximately 30% of the background while retaining approximately 99% of the $t\bar{t}$ signal. No H_T requirement is made for the control region of 1- and 2-jet events.

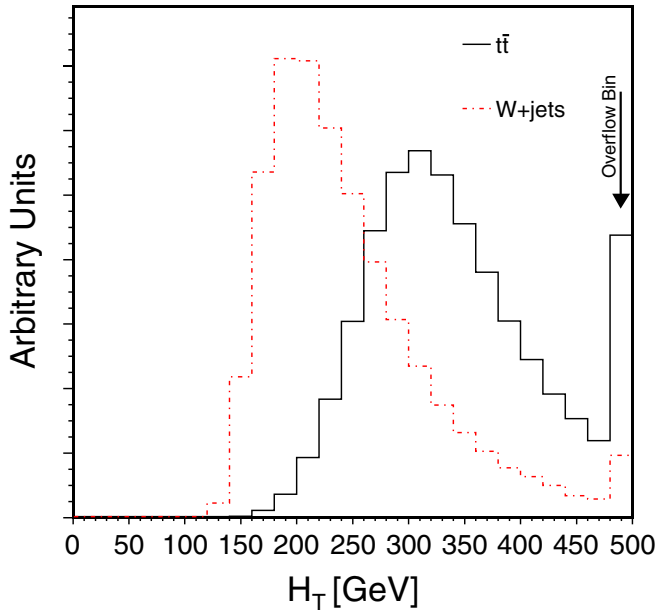

FIG. 2 (color online). The distribution of H_T for simulated $t\bar{t}$ and W + jets events with at least three jets.

B. Muon tagging

Even after the H_T requirement is imposed, the expected signal to background ratio in $W+ \geq 3$ jet events is about 1:7. To further improve the signal to background ratio, events with one or more b-jets are identified by searching inside jets for semileptonic decays of b-hadrons into muons. The algorithm for identifying such candidate b-jets is known as soft-lepton tagging or "SLTμ" and a jet with a candidate semileptonic b decay to a muon is a "tagged" jet. The SLTμ algorithm is described in detail in Ref. [4]. We review here only its basic features.

Muon identification at CDF relies on the presence of a track segment ("stub") in the muon chambers, matched to a track in the central tracking system. The soft muon tagger is based on a χ^2 function that uses all available information about the match between the extrapolated COT track and the muon stub to require that the deviations be consistent with the multiple Coulomb scattering expected for a muon traversing the CDF calorimeter.

The algorithm begins by selecting "taggable" tracks. A track is declared taggable if it contains at least 3 axial and 2 stereo COT superlayers that have at least 5 hits each. To obtain some rejection for decays in flight (DIF), the impact parameter, d_0, of the track with respect to the beam line, is required to be less than 2 mm. The track is further required to originate within 60 cm of the center of the detector along the beam direction. Finally, the track must have a P_T above an approximate range-out threshold of 3.0 GeV/c and extrapolate to within a fiducial volume at the muon chambers that extends $3\sigma_{\mathrm{MS}}$ outside of the physical edges of the chambers, where σ_{MS} is the deviation expected from multiple Coulomb scattering at the track P_T.

Matching between the extrapolated COT track and the muon stub is done using the following observables ("matching variables"): the extrapolated position along the muon chamber drift direction (x), the longitudinal coordinate along the chamber wires (z) when such information is available, and the extrapolated slope (ϕ_L). Tracks in the COT are paired with stubs based on the best match in x, which must be less than 50 cm for a track-stub pair to become a muon candidate. We refer to the difference between the extrapolated and measured positions in x and z as Δx and Δz, respectively, and between the extrapolated and measured slope as $\Delta\phi_L$. The distributions of these variables over an ensemble of events are referred to as the "matching distributions."

Candidate muons are selected with the SLTμ algorithm by constructing a global χ^2 quantity, L, based on a comparison of the measured matching variables with their expectations. The first step in constructing L is taking a sum, Q, of individual χ^2 variables:

$$Q = \sum_{i=1}^{n} \frac{(X_i - \mu_i)^2}{\sigma_i^2}, \tag{1}$$

where μ_i and σ_i are, respectively, the expected mean and width of the distribution of the matching variable X_i. The sum is taken over n selected variables as described below. We construct L, by normalizing Q according to

$$L = \frac{(Q - n)}{\sqrt{\mathrm{var}(Q)}}, \tag{2}$$

where the variance, var(Q), is calculated using the full covariance matrix for the selected variables. The normalization is chosen to make L independent of the number of variables n.

The selected variables are the full set of matching variables, Δx, Δz, and $\Delta\phi_L$ in the CMU, CMP, and CMX with the following two exceptions: The CMP chambers do not provide a measurement of the longitudinal coordinate z, and matching in ϕ_L is not included for stubs in the muon chambers that have only three hits. Because of their significantly poorer resolution, track segments reconstructed only in the CMU or only in the CMP chambers with only three hits are rejected (if the SLTμ candidate has stubs in both CMU and CMP, then a stub with only three hits is allowed). These two exceptions are a new feature of the algorithm, since the previous publication, that reduce backgrounds from hadronic punchthrough with a negligible effect on the efficiency. Note that a muon that traverses both the CMU and the CMP chambers yields two sets of matching measurements in x and ϕ_L and one z matching measurement, and is referred to as a CMUP muon. All available matching variables are used in the calculation of L for a given muon candidate.

As described in Ref. [4], the expected means and widths in Eq. (1) are parametrized as a function of the P_T of the muon using J/ψ and W and Z bosons in the data. We use the same parametrization described there. The efficiency has been remeasured, from the data, using the full data set for this analysis.

Using J/ψ events only, we measure the efficiency as a function of the quantity L defined in Eq. (2) (the efficiency measurement is described in detail in Sec. V B). The efficiency plateaus at a value of $|L| \leq 3.5$, and we therefore use this requirement to define an SLTμ tag.

Beginning with the W + jets candidate data set, selected as described in Sec. III A, we require that at least one jet in each event has an SLTμ tag. A jet is determined to have an SLTμ tag if a candidate muon with $|L| \leq 3.5$ is found within a cone of $\Delta R < 0.6$ centered on the jet axis. When the primary lepton is a muon, the event is rejected when the SLTμ has opposite charge to the primary muon and together with that muon has an invariant mass between 8 and 11 GeV/c^2 or between 70 and 110 GeV/c^2. This rejects events in which an Υ or Z boson decays to a pair of muons, one of which becomes the primary lepton while the other ends up in a jet and is tagged by the SLTμ algorithm. Whether the primary is an electron or a muon, events where the invariant mass is less than 5 GeV/c^2 are also removed to prevent sequential double-semileptonic

$b \to c \to s$ decays (where the primary lepton and the SLTμ tag are from these semileptonic decays, rather than the primary lepton being from the decay of a W boson) from entering the sample, as well as events with a J/ψ decay. We further reject events as candidate radiative Drell-Yan and Z bosons if the tagged jet has an electromagnetic energy fraction above 0.8 and only one track with >1.0 GeV$/c$ within a cone of $\Delta R = 0.4$ about the jet axis.

Three levels of selection are defined in this analysis. Events that pass the kinematic cuts and the dilepton and radiative-Z vetoes, but do not necessarily have an SLTμ-taggable track in them, comprise the ''pretag'' sample. Pretag events that have an SLTμ-taggable track ($P_T > 3$ GeV$/c$, passing quality cuts, pointing to the muon chambers) within $\Delta R < 0.6$ of a jet with $E_T >$ 20 GeV are called taggable events. Finally, the subset of SLTμ-taggable events that have at least one SLTμ-tagged jet are called tagged events.

C. Selected event samples

Table I shows the number of pretagged, taggable, and tagged events in the electron and muon channels in this data set as a function of jet multiplicity.

IV. MONTE CARLO DATA SETS

The detector acceptance of $t\bar{t}$ events is modeled using PYTHIA v6.216 [8] and HERWIG v.6.510 [9]. This analysis uses the former for the final cross section estimate and the latter to estimate the systematics resulting in the modeling of $t\bar{t}$ production and decay. The PYTHIA event generator has been tuned using jet data to better model the effects of multiple interactions and remnants from the breakup of the proton and antiproton. The generators are used with the CTEQ5L parton distribution functions [10]. Decays of b- and c-hadrons are modeled using EVTGEN [11].

TABLE I. Summary of event counts for 2 fb^{-1} of CDF run II data for the event selection described in Secs. III A and III B.

	1 jet	2 jets	3 jets	≥ 4 jets	≥ 3 jets
			Electrons		
Pretag	79 348	13 068	1615	660	2275
SLTμ taggable	43 005	10 479	1518	648	2166
SLTμ tagged	519	224	85	64	149
			CMUP muons		
Pretag	38 165	6 320	719	325	1044
SLTμ taggable	20 162	4 921	673	312	985
SLTμ tagged	224	105	41	34	75
			CMX muons		
Pretag	23 503	3 672	422	162	584
SLTμ taggable	12 428	2 864	396	160	556
SLTμ tagged	149	55	16	8	24
			Electrons + muons		
Pretag	141 016	23 060	2756	1147	3903
SLTμ taggable	75 595	18 264	2587	1120	3707
SLTμ tagged	892	384	142	106	248

Events with a W boson produced in association with multiple jets are modeled using ALPGEN v2.1 [12], with parton showering provided by PYTHIA v6.326 and HF hadron decays handled by EVTGEN. ALPGEN calculates exact matrix elements at leading order for a large set of parton level processes in QCD and electroweak interactions. The showering in PYTHIA may result in multiple ALPGEN samples covering the same phase space. These overlaps are removed using a jet-parton matching algorithm along with a jet-based heavy-flavor overlap removal algorithm [13].

Estimates of backgrounds from diboson production (WW, WZ, and ZZ) and Drell-Yan$/Z \to \tau\tau$ are derived using PYTHIA. Drell-Yan to $\mu\mu$ events are modeled using ALPGEN with PYTHIA showering while single-top production is modeled with MADEVENT [14], also with PYTHIA showering.

The CDF II detector simulation reproduces the response of the detector to particles produced in $p\bar{p}$ collisions. The detector geometry database used in the simulation is the same as that used for reconstruction of the collision data. Details of the CDF II simulation can be found in [15].

V. EFFICIENCY FOR IDENTIFYING $t\bar{t}$ EVENTS

The efficiency for identifying $t\bar{t}$ events in this analysis is factorized into the geometric times kinematic acceptance and the SLTμ tagging efficiency. The acceptance is evaluated assuming a top mass of 175 GeV$/c^2$ and includes the branching fraction to leptons, which is assumed to have the SM value. The tagging efficiency is the efficiency for SLTμ tagging at least one jet in events that pass the geometric and kinematic selection. Each piece is described below.

A. Geometric and kinematic acceptance

The acceptance of $t\bar{t}$ events in this analysis is measured in PYTHIA and then corrected, using measurements from the data, for effects that are not sufficiently well modeled in the simulation: the lepton trigger efficiencies, the fraction of the $p\bar{p}$ luminous region well contained in the CDF detector (i.e., the z-vertex cut efficiency), and track reconstruction and lepton identification efficiencies. The efficiency of the z-vertex cut, $|z_0| < 60$ cm, is measured from minimum-bias triggered events to be $(96.3 \pm 0.2)\%$. The correction factor for the difference between the track reconstruction efficiencies in data and simulation is 1.014 ± 0.002. Events in the Monte Carlo (MC) samples are not required to pass any trigger, so the acceptance is multiplied by lepton trigger efficiency. The lepton trigger and identification efficiencies, measured using the unbiased leg of Z boson decays to electrons and muons, and the correction

TABLE II. Summary of lepton trigger and identification efficiencies.

Quantity	Electron	CMUP muon	CMX muon
Trigger efficiency	0.966 ± 0.005	0.917 ± 0.005	0.925 ± 0.007
Lepton ID efficiency (data)	0.789 ± 0.004	0.829 ± 0.006	0.893 ± 0.006
Lepton ID efficiency (MC)	0.806 ± 0.001	0.896 ± 0.001	0.916 ± 0.002
Lepton ID correction	0.978 ± 0.005	0.926 ± 0.007	0.975 ± 0.007

TABLE III. Acceptance for $t\bar{t}$ events as a function of jet multiplicity from the PYTHIA Monte Carlo sample, after data/MC corrections described in the text. In the combined acceptance we account for the fact that the CMX detector was not operating early in run II. The uncertainties listed are statistical only.

	1 jet	2 jets	3 jets	≥ 4 jets	≥ 3 jets
Electron (%)	0.163 ± 0.002	0.858 ± 0.004	1.63 ± 0.01	2.08 ± 0.01	3.71 ± 0.01
CMUP muon (%)	0.088 ± 0.001	0.472 ± 0.003	0.909 ± 0.004	1.142 ± 0.005	2.05 ± 0.01
CMX muon (%)	0.042 ± 0.001	0.219 ± 0.002	0.414 ± 0.003	0.532 ± 0.003	0.946 ± 0.004
Combined (%)	0.292 ± 0.002	1.544 ± 0.005	2.946 ± 0.008	3.743 ± 0.009	6.69 ± 0.01

factors for each of the primary lepton types are shown in Table II.

The raw acceptance is defined as the number of pretag events divided by the total number of $t\bar{t}$ events in the PYTHIA sample. The acceptance, after correcting for the differences between data and simulation, is shown in Table III as a function of the number of identified jets.

B. Efficiency of the SLTμ algorithm

The efficiency of the SLTμ algorithm is measured from the data using samples of J/ψ and Z decays triggered on a single muon. The tagger is applied to the nontrigger muon (probe leg). If both legs pass the trigger, only one of them is used. To reduce background in the Z sample, the leg that is not used to measure efficiency is required to be isolated and to be consistent with being a minimum ionizing particle in the calorimeter. We correct for the remaining background using the invariant mass regions outside the Z mass window ("sidebands").

The efficiency of the SLTμ is defined as

$$\epsilon = \frac{\text{No. of tagged muons}}{\text{No. of taggable muon tracks with a stub}}. \quad (3)$$

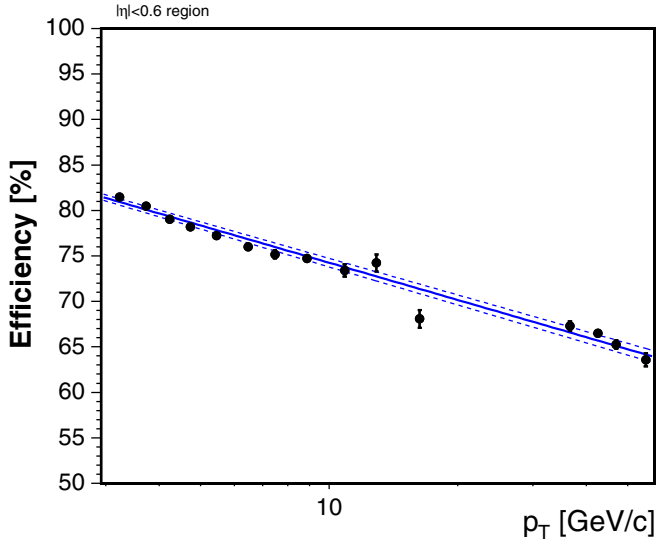

FIG. 3 (color online). The SLTμ efficiency for CMU/CMP as a function of P_T measured from J/ψ and Z data for $|L|<3.5$. The solid line is the fit to the data and the dashed lines indicate the uncertainty on the fit.

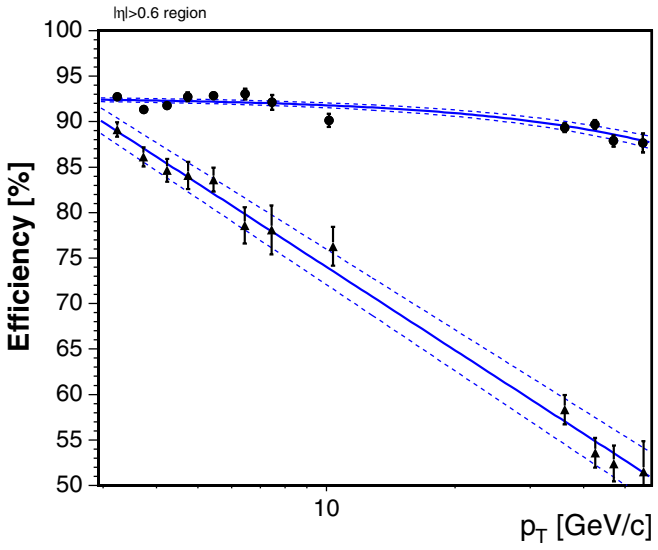

FIG. 4 (color online). The SLTμ efficiency for CMX arches (circles) and miniskirt/keystone (triangles) as a function of P_T measured from J/ψ and Z data for $|L|<3.5$. The solid curves are the fits to the data and the dashed lines indicate the uncertainties on the fits.

TABLE IV. $t\bar{t}$ event tagging efficiency for SLT muons as a function of jet multiplicity from the PYTHIA Monte Carlo sample. The lepton category refers to the primary lepton. The average tagging efficiency is determined by weighting each channel by the acceptance and luminosity for each channel. The listed uncertainties are statistical only.

	1 jet	2 jets	3 jets	≥ 4 jets	≥ 3 jets
Electron (%)	7.0 ± 0.3	11.4 ± 0.2	12.9 ± 0.1	14.9 ± 0.1	14.0 ± 0.1
CMUP muon (%)	5.6 ± 0.3	10.7 ± 0.2	11.8 ± 0.1	14.1 ± 0.1	13.1 ± 0.1
CMX muon (%)	6.7 ± 0.5	11.2 ± 0.3	12.3 ± 0.2	14.2 ± 0.2	13.4 ± 0.2
Average (%)	6.5 ± 0.2	11.2 ± 0.1	12.5 ± 0.1	14.6 ± 0.1	13.6 ± 0.1

The requirement in the denominator that the taggable muon track has a stub in the requisite muon chambers decouples the muon reconstruction efficiency, which is accounted for separately, from the efficiency of the tagger. Figures 3 and 4 show the efficiency for tagging muons with $|L| \leq 3.5$ as a function of muon P_T from both J/ψ and Z data. The decrease in efficiency with increasing P_T is due, primarily, to non-Gaussian tails in the resolution functions. These efficiency data are fit to functional forms [4] shown as the curves in the data. The dotted curves are those obtained by varying the fit parameters by $\pm 1\sigma$. Although the efficiency measurement is dominated by isolated muons, we do not expect that it will depend on the isolation of the muon because the muon chambers are well shielded from the inner detector. We have checked this assumption by measuring the efficiency as a function of the number of nearby tracks and found no dependence.

The efficiency for SLTμ tagging a $t\bar{t}$ event is measured for Monte Carlo events that pass the geometric and kinematic selection. We model the SLTμ tagging in these events by tagging muons from semileptonic HF decay with a probability given by the efficiencies in Figs. 3 and 4. Events without a ''real'' muon tag of this type can still be SLTμ tagged through a mistag. Mistags in $t\bar{t}$ events are included by applying the ''mistag matrix'' described in the following section, and are included as part of the signal efficiency. The SLTμ tagging efficiency in $t\bar{t}$ events is given in Table IV.

VI. PREDICTING THE NUMBER OF TAGS FROM LIGHT-QUARK JETS

As a prelude to the evaluation of the backgrounds to the $t\bar{t}$ signal we describe a new method, developed for this analysis, for predicting the number of SLTμ tags that come from light-quark jets. We refer to these as mistags, and they result from a combination of hadronic punch-through of the calorimeter and muon steel, and hadronic decays in flight.

To predict the number of mistags in our sample we use a track-based mistag probability that is a function of track P_T and η. We use reconstructed D^* and Λ^0 to identify a clean sample of pions, kaons, and protons and measure the probability per taggable track, in 8 bins of P_T and 9 bins of η, for each to satisfy the SLTμ $|L| < 3.5$ requirement. Details of the reconstruction technique, the measurement of the tagging probabilities, and the assembly and testing of the two-dimensional (8×9) mistag matrix are described in what follows.

A. Data samples

To identify kaons and pions we reconstruct $D^{*+} \rightarrow D^0\pi^+ \rightarrow K^-\pi^+\pi^+$ decays, and their charge conjugates. This data set is collected using a two-track trigger that requires two oppositely charged tracks with $P_T \geq 2$ GeV/c. The tracks are also required to have a scalar sum $P_{T1} + P_{T2} \geq 5.5$ GeV/c, an opening angle between them of $2^\circ \leq |\Delta\phi| \leq 90^\circ$, and originate from a displaced vertex.

A sample of protons is obtained by reconstructing $\Lambda \rightarrow p\pi^-$ decays. These events are collected using another two-track trigger similar to the one described above, but with an opening angle requirement of $20^\circ \leq |\Delta\phi| \leq 135^\circ$ and the invariant mass of the track pair (assumed to be pions) required to be 4 GeV/$c^2 \leq M(\pi, \pi) \leq 7$ GeV/c^2.

B. Event reconstruction

We apply the following track quality criteria in the reconstruction of both D^* [16] and Λ^0 [17] decays:

(i) the number of COT axial superlayers with ≥ 5 hits is ≥ 3;
(ii) the number of COT stereo superlayers with ≥ 5 hits is ≥ 2;
(iii) the track has $|z_0| \leq 60$ cm.

The D^* reconstruction then proceeds through the examination of the mass difference $\Delta m = m(K\pi\pi) - m(K\pi)$ with the following criteria:

(i) the kaon must have opposite charge to each of the two pions;
(ii) $|\Delta z_0| \leq 5$ cm between any two tracks;
(iii) the soft pion from the $D^* \rightarrow D^0\pi$ decay must have $P_T \geq 0.5$ GeV/c;
(iv) the kaon and pion from the D^0 decay must each have $P_T \geq 2$ GeV/c;
(v) the kaon and pion tracks must have impact parameter, $|d_0| \leq 0.2$ cm;
(vi) $|m(K\pi) - m(D^0)| \leq 0.03$ GeV/c^2;

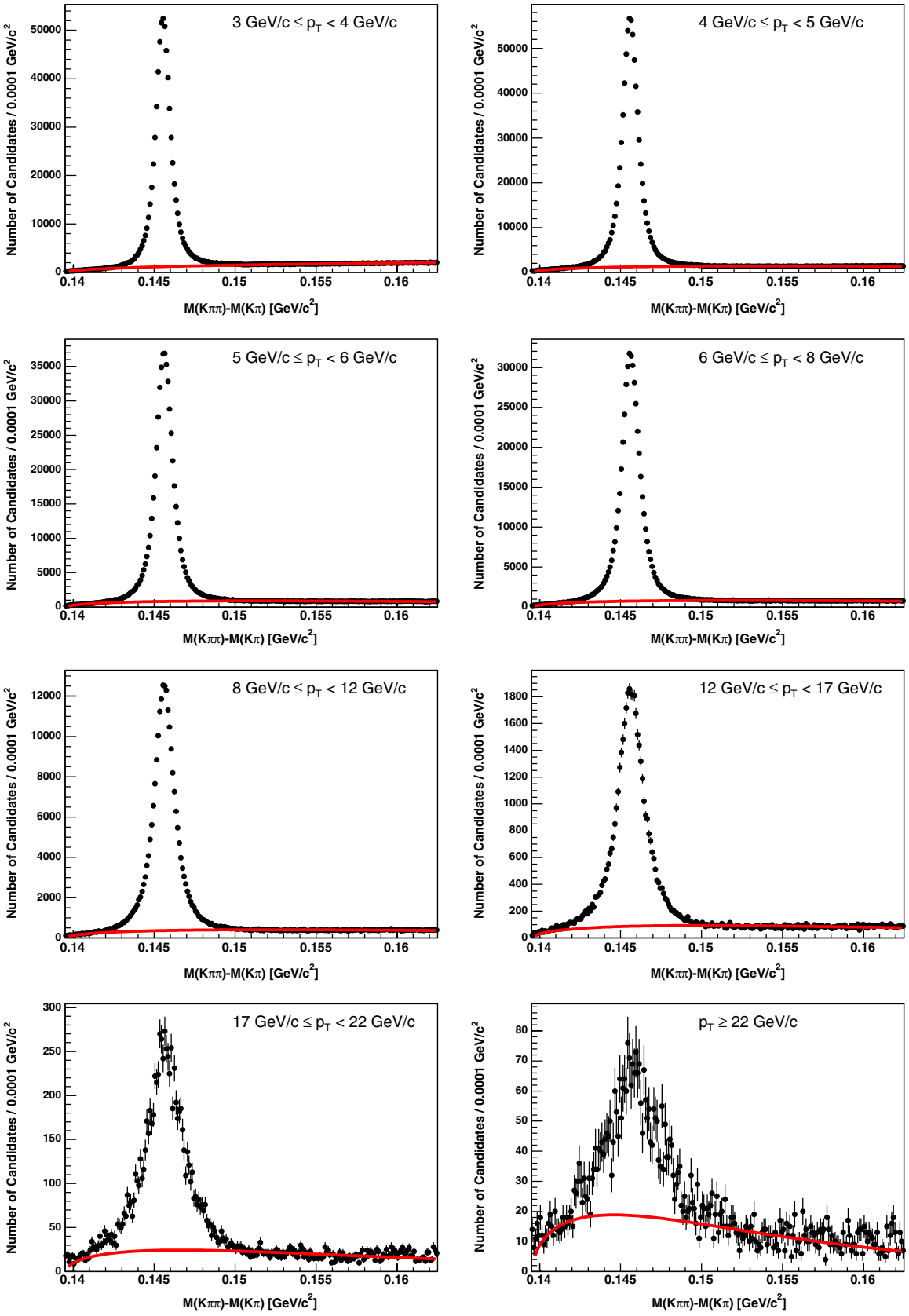

FIG. 5 (color online). The $m(K\pi\pi) - m(K\pi)$ distribution for $D^{*\pm} \to D^0\pi^\pm$, $D^0 \to K^\mp\pi^\pm$ candidates in different SLTμ-track-P_T bins. The line in each plot represents the fit to the sideband regions.

(vii) At least one of the tracks (K or π) from the D^0 must be SLTμ taggable (including having $P_T \geq 3$ GeV/c).

As shown in Fig. 5, a clean D^* signal is obtained for the right-sign Δm distribution.

The reconstruction of Λ decays requires the following criteria:

(i) the pion and proton must have opposite charge;
(ii) $|\Delta z_0| \leq 2$ cm between the two tracks;
(iii) the χ^2 of the vertex fit must be ≤ 10;
(iv) the vertex must have $L_{xy} \geq 0.5$ cm, where L_{xy} is defined as the projection onto the net momentum direction, in the $r - \phi$ plane, of the vector pointing from the primary to the secondary vertex;
(v) the proton P_T is greater than the pion P_T;
(vi) the pion must have $P_T \geq 0.4$ GeV/c;
(vii) the proton must have $|d_0| \leq 0.2$ cm;
(viii) the proton must be SLTμ taggable (including having $P_T \geq 3$ GeV/c).

Figure 6 shows the invariant mass distribution in the $p\pi$ mass hypothesis.

We define a signal region for D^* and Λ^0 decays as well as sideband regions for each. We measure the sideband-subtracted tagging probability for K, π, and p tracks using

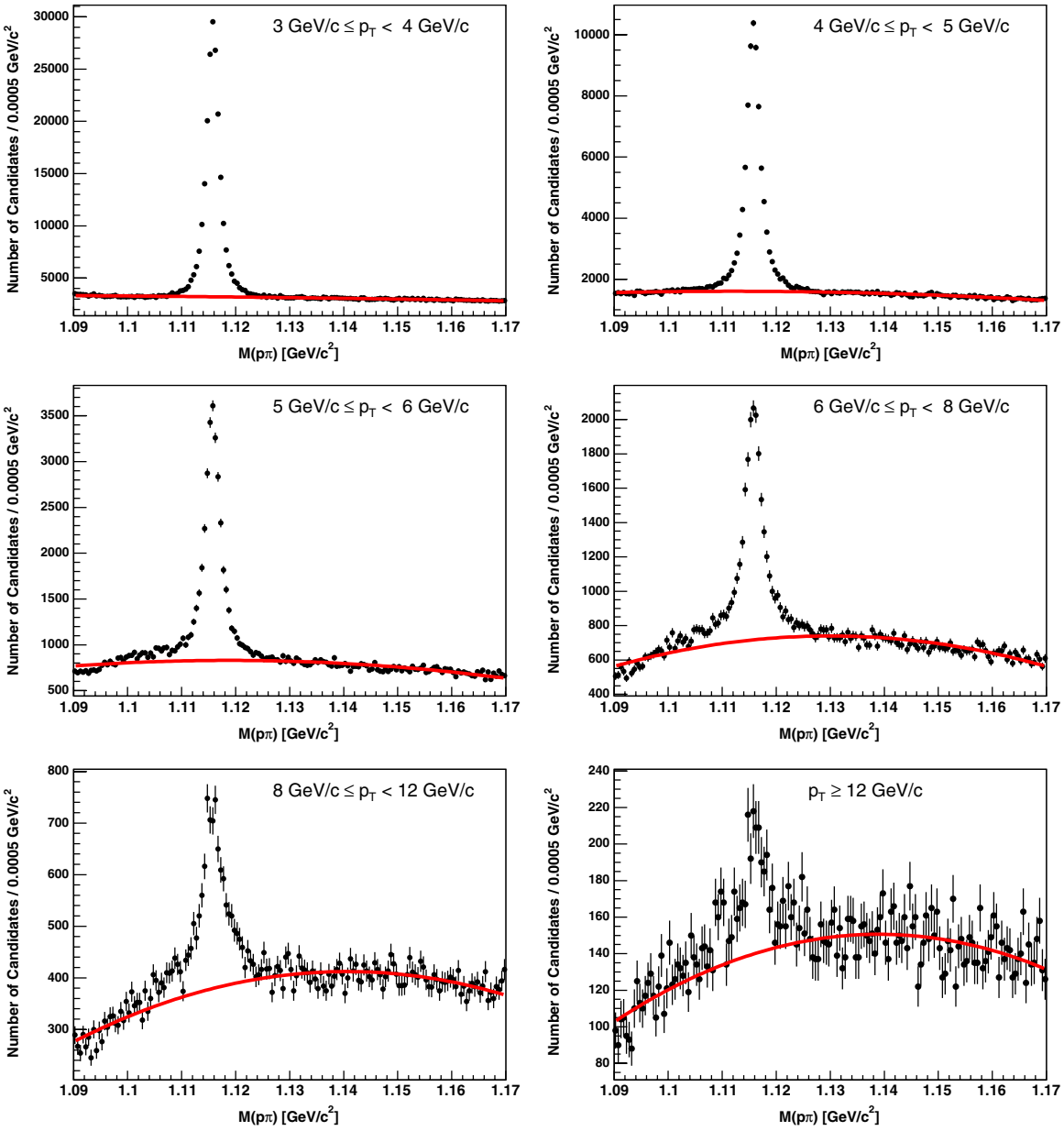

FIG. 6 (color online). The $m(p\pi)$ distribution for $\Lambda^0 \rightarrow p\pi$ candidates in different SLTμ-track-P_T bins. The line in each plot represents the fit to the sideband regions.

TABLE V. Mass windows used in determining the status of a D^* or Λ^0 candidate.

Region	Mass window (MeV/c^2)
D^* signal	$142.421 < \Delta m < 148.421$
D^* sidebands	$139.6 < \Delta m < 141$ or $152 < \Delta m < 162.5$
Λ^0 signal	$1109.683 < m < 1121.683$
Λ^0 sidebands	$1090 < m < 1105.683$ or $1125.683 < m < 1170$

events in the signal, corrected for the enhanced probabilities in the sidebands. The sideband regions have a higher SLTμ per track tag probability because they are enriched in HF as a result of the two-track trigger described above. The signal and sideband regions are given in Table V and the sideband subtraction is done using the fits [5] shown in Figs. 5 and 6. The tag probabilities before and after sideband subtraction are shown as a function of P_T in Fig. 7. We note that there are systematic uncertainties due to the choice of fit functions and, in particular, the quality of the fits in the sideband regions. These systematics, and all others associated with the construction of the mistag matrix, are evaluated by testing the predictive power of the matrix on a variety of independent data samples, as described in Sec. VIII B.

The mistag matrix is designed to predict SLTμ tags that arise from both hadronic punchthrough and decays in flight. When a pion or a kaon from a D^* decays in flight, the track may be poorly reconstructed causing the reconstructed mass to fall outside of the signal region defined in Table V. We measure the size of this effect using D^* decays in a Monte Carlo sample and make a correction. The correction factor is calculated in three bins in P_T (limited by the Monte Carlo sample size) and shown in Table VI. Full details of the calculation of the correction factor are given in [5].

C. The mistag matrix

At this point we have SLTμ tag probabilities for tracks from π, K, and p, corrected for backgrounds (sideband subtracted) and for a bias against π and K decays in flight. What remains is to assemble these separate SLTμ tag probabilities into a full mistag matrix that can be used to predict the number of tags in light-flavor jets in W + jets events.

To assemble the final mistag matrix, we take a weighted sum of the individual π, K, and p matrices as follows:

$$M_{ij} = W_\pi \cdot M^\pi_{ij} + W_K \cdot M^K_{ij} + W_p \cdot M^p_{ij}, \qquad (4)$$

where M_{ij} is the entry in the ith P_T and jth η bins of the final matrix and M^π_{ij}, M^K_{ij}, and M^p_{ij} are the corresponding entries in the π, K, and p matrices. The weights $W_\pi = 71.9\%$, $W_K = 15.6\%$, and $W_p = 12.5\%$ are taken from the taggable-track particle content of light-quark jets in

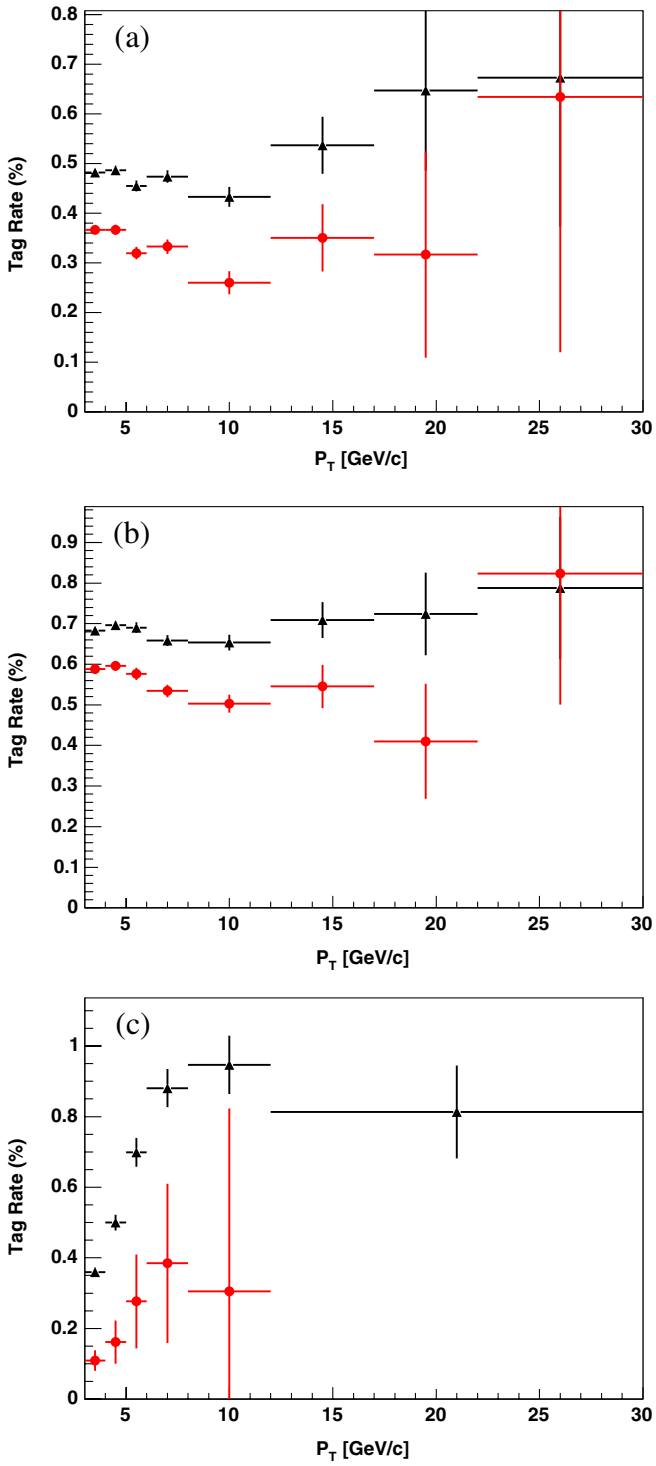

FIG. 7 (color online). The measured (triangles) and sideband-subtracted (circles) tag probabilities as a function of track P_T for (a) pions, (b) kaons, and (c) protons. The uncertainties shown are statistical only.

ALPGEN W + jets Monte Carlo events. Figure 8 shows the final tag probability for the eight P_T bins (integrated over η) and the nine η bins (integrated over P_T). The features in the η distribution are due to the profile of

TABLE VI. Relevant numbers, from Monte Carlo simulation, in the determination of the decay-in-flight correction for D^* decays. These include the fraction of taggable tracks from D^*s that decay in flight (DIF), the same fraction after all reconstruction requirements that fall inside the D^* signal window (shown in Table V) and the probability for tagging a decay in flight. The last column gives the correction factor that is applied to the measured tag probability to account for the bias against decays in flight.

	P_T (GeV/c)	Frac. DIF (%)	After reco. (%)	DIF tag prob. (%)	Corr. factor
	3–4	0.40 ± 0.05	0.20 ± 0.04	44.6 ± 2.0	1.25 ± 0.08
π	4–6	0.25 ± 0.04	0.16 ± 0.03	60.1 ± 2.3	1.16 ± 0.08
	>6	0.20 ± 0.04	0.16 ± 0.04	75.6 ± 2.6	1.09 ± 0.14
	3–4	0.99 ± 0.09	0.77 ± 0.08	10.2 ± 1.3	1.04 ± 0.02
K	4–6	0.65 ± 0.06	0.51 ± 0.06	10.8 ± 1.3	1.02 ± 0.02
	>6	0.39 ± 0.05	0.23 ± 0.04	18.2 ± 1.8	1.05 ± 0.02

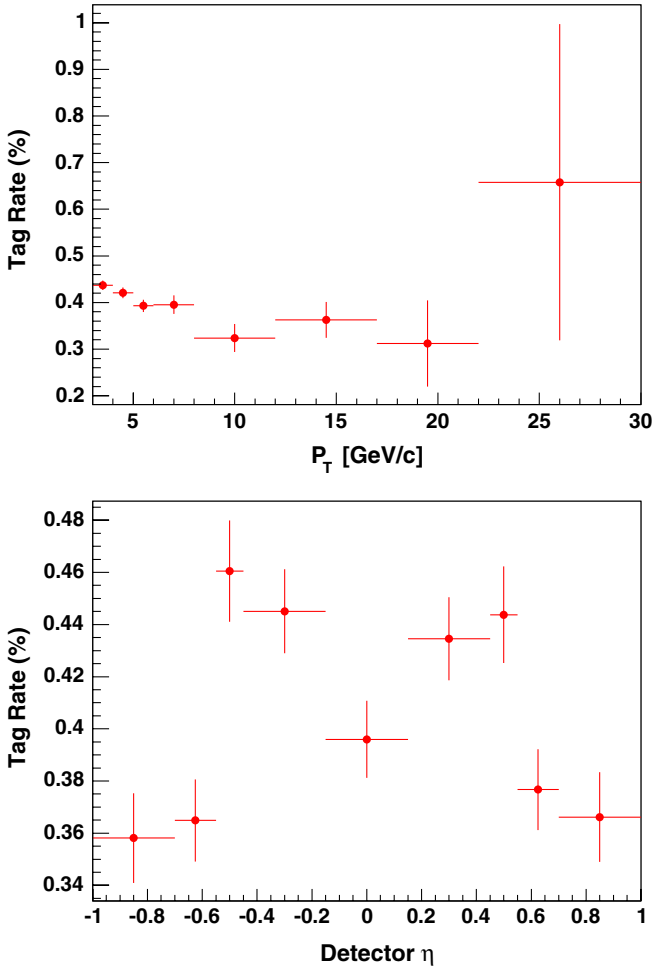

FIG. 8 (color online). The mistag probability per track as a function of track P_T and detector η. The histogram binning matches that of the matrix. The uncertainties shown are statistical only. The structure in the η distribution is an artifact of the profile of the absorber and geometrical coverage of the muon system.

absorber in front of, and the coverage of, the muon system. The average tag probability per track in the matrix is $(0.41 \pm 0.01)\%$ per track.

The uncertainties associated with the probabilities in the mistag matrix include uncertainties from the sideband subtraction, the decay-in-flight correction, and the weighting of π, K, and p probabilities, to name just a few. To evaluate the overall systematic uncertainty on the number of light-quark tags predicted by the matrix, one possibility would be to carefully evaluate the size of each of these uncertainties. However, there is no straightforward way to do this. Instead, as described in detail in Sec. VIII B, we directly test the predictive power of the matrix, using event samples acquired with jet triggers, and use the control samples of $W + 1$ and 2 jet events to further validate the technique and establish that we have not underestimated the size of the systematic uncertainty.

VII. BACKGROUND EVALUATION

The dominant background contribution to the $t\bar{t}$ signal in this analysis comes from mistags in $W +$ jets events. Another smaller, yet still significant background comes from W bosons produced in association with heavy flavor ($Wb\bar{b}$, $Wc\bar{c}$, and Wc). The estimate of the mistag background is described in Sec. VII A, while the $W +$ HF background estimate is described in Sec. VII B.

Other backgrounds that can produce a W boson and an SLTμ tag that are not accounted for by the mistag matrix include dibosons (WW, ZZ, WZ), $Z \to \tau^+\tau^-$, single top, QCD multijet backgrounds including $b\bar{b}$, and residual Drell-Yan ($\mu\mu$) events not removed by the dimuon removal. QCD and Drell-Yan backgrounds are measured using the data, as described in detail in Secs. VII C and VII Dbelow. The remaining backgrounds are estimated from Monte Carlo samples as described in Sec. VII E. We treat QCD independently of the calculation of mistags in $W +$ jets events because events that enter our sample by mimicking the signature of a W boson can have a signifi-

cantly larger tag rate than true W events. The enhanced tag rate arises due to the contribution of $b\bar{b}$ events to the QCD background and because of the correlation between the tag rate and measured $\not\!\!E_T$ in events in which the $\not\!\!E_T$ arises from jet mismeasurement or semileptonic HF decay rather than from a neutrino in a W boson decay. In order to avoid double counting we correct the estimate of tags in W + jets events by $(1 - F_{\rm QCD})$, where $F_{\rm QCD}$ is the QCD multijet fraction in the W + jets candidate sample.

A. Mistags

The background due to mistags is evaluated using the track-based mistag matrix described in Sec. VI. To predict the number of events from W + jets with at least 1 mistag, we apply the mistag matrix to all pretag events according to

$$N_{\rm raw}^{\rm Wjtag} = \sum_{\rm events}\left[1 - \prod_{i=1}^{N_{\rm trk}}(1 - \mathcal{P}(P_{Ti}, \eta_i))\right], \qquad (5)$$

where the sum runs over each event in the pretag sample, and the product is over each taggable track in the event. $\mathcal{P}(P_{Ti}, \eta_i)$ is the probability from the mistag matrix for tagging the ith track with parameters P_{Ti} and η_i. Note that the sum over the events in Eq. (5) includes any $t\bar{t}$ events that are in the pretag sample. We correct for the resulting overestimate of the background at the final stage of the cross section calculation (see Sec. IX). It also includes W + HF events, diboson events, etc. Therefore mistags from these backgrounds are included here. Tags from muons resulting from the decay of HF hadrons or W or Z bosons in these backgrounds are calculated separately using Monte Carlo simulations, as described in Secs. VII B and VII E. To avoid any double counting the Monte Carlo estimates of the contributions from these backgrounds do not include any mistags.

A fraction, $F_{\rm QCD}$, of the events in the signal region are QCD events for which the background is estimated separately. Therefore, we correct the prediction of Eq. (5) according to

$$N_{\rm corr}^{W\,j\rm tag} = (1 - F_{\rm QCD}) \cdot N_{\rm raw}^{W\,j\rm tag}. \qquad (6)$$

The background estimate from the application of the mistag matrix is shown in Table VII. We list here both the raw prediction and that corrected by $(1 - F_{\rm QCD})$. The calculation of $F_{\rm QCD}$ is described in Sec. VII C 1.

B. W + heavy flavor

The evaluation of background tags from the semileptonic decays of HF quarks in $Wb\bar{b}$, $Wc\bar{c}$, and Wc events is done using the ALPGEN Monte Carlo program. We determine the fraction of W + jets events that contain heavy flavor at the pretag level, $F_{\rm HF}$, and the tagging efficiency, $\epsilon_{\rm HF}$, for these events and then normalize the total to the number of W + jets events seen in the data. The final prediction of the number of tags from W + heavy-flavor events is

$$N_{\rm HF} = (1 - F_{\rm QCD} - F_{\rm other}) \cdot N_{\rm pretag} \cdot F_{\rm HF} \cdot \epsilon_{\rm HF}, \qquad (7)$$

where $F_{\rm QCD}$ is the fraction of QCD events in the pretag sample and $F_{\rm other}$ is the fraction of other, non-W + jets backgrounds. As with the mistag prediction, correction for $t\bar{t}$ in the pretag sample is done as part of the final cross section calculation.

This procedure is used because the theory cross sections for the $Wb\bar{b}$, $Wc\bar{c}$, and Wc processes have large uncertainties, whereas the uncertainties on the fraction of events with heavy-flavor jets are smaller. This procedure follows that used in [3].

The HF fractions of events in the W + jets sample are determined by measuring the fractions in Monte Carlo events and then scaling those fractions by a multiplicative factor of 1.15 ± 0.35, determined by comparing measured HF fractions in inclusive jet data with those predicted by ALPGEN.

The ALPGEN HF fractions, broken down according to the number of b- or c-jets, are shown in Table VIII. In addition to the uncertainty on the HF-fraction scaling, an additional uncertainty on the ALPGEN fractions is determined by varying the ALPGEN generator parameters such as Q^2 and the quark masses.

The Monte Carlo sample is also employed to determine the efficiency for tagging a muon from a semileptonic heavy-flavor decay in W + heavy-flavor events. As with the $t\bar{t}$ tagging efficiency described in Sec. V, tags are assigned based on the SLTμ tagging efficiency measured in the data (Figs. 3 and 4). The results are shown in Table VIII. Note that we do not include here the additional efficiency that arises from mistags in real HF jets, because this is included in the mistag evaluation given in Table VII.

Armed with these HF fractions and tagging efficiencies, the number of tagged events from W + HF is evaluated

TABLE VII. Summary of background estimate from mistags in W + jets events. These numbers include a contribution from $t\bar{t}$ events in the W + jets sample that is removed in the final cross section calculation, as described in Sec. IX.

	1 jet	2 jet	3 jets	≥ 4 jets	≥ 3 jets
$N_{\rm raw}^{W\,j\rm tag}$	641.0 ± 32.0	238.0 ± 12.0	55.0 ± 2.8	32.7 ± 1.6	87.5 ± 4.4
$N_{\rm corr}^{W\,j\rm tag}$	622.0 ± 31.0	226.0 ± 12.0	53.0 ± 2.7	31.4 ± 1.6	84.5 ± 4.3

TABLE VIII. The heavy-flavor fractions, F_{HF}, tagging efficiencies, ϵ_{HF}, and W + heavy-flavor background evaluated using the ALPGEN Monte Carlo simulation. The fractions are scaled by 1.15 as described in the text. The uncertainty on the heavy-flavor fractions includes that from the scaling factor and from variation of the ALPGEN parameters.

	1 jet	2 jets	3 jets	≥ 4 jets	≥ 3 jets
		Category 2 b			
F_{HF} (%)		0.9 ± 0.3	1.8 ± 0.7	2.8 ± 1.1	2.0 ± 0.8
ϵ_{HF} (%)		7.8 ± 0.2	8.4 ± 0.2	8.5 ± 0.3	8.4 ± 0.2
		Category 1 b			
F_{HF} (%)	0.7 ± 0.3	1.4 ± 0.5	2.6 ± 1.0	3.0 ± 1.1	2.7 ± 1.0
ϵ_{HF} (%)	3.54 ± 0.05	4.30 ± 0.06	5.5 ± 0.1	5.8 ± 0.2	5.53 ± 0.09
		Category 2 c			
F_{HF} (%)		1.3 ± 0.5	2.8 ± 1.1	4.5 ± 1.7	3.1 ± 1.2
ϵ_{HF} (%)		3.1 ± 0.1	3.6 ± 0.1	3.5 ± 0.2	3.6 ± 0.1
		Category 1 c			
F_{HF} (%)	5.5 ± 2.1	8.9 ± 3.4	11.0 ± 4.1	11.5 ± 4.4	11.1 ± 4.2
ϵ_{HF} (%)	1.52 ± 0.02	1.70 ± 0.03	2.04 ± 0.07	2.05 ± 0.06	2.04 ± 0.06
$Wb\bar{b} + Wc\bar{c} + Wc$ background	145 ± 55	66.6 ± 25.2	15.3 ± 5.8	8.5 ± 3.2	23.0 ± 8.7

according to Eq. (7). The results are given in the last line of Table VIII.

C. QCD background

The background due to tags in QCD events that enter the signal sample is estimated by calculating the fraction of QCD events in the W + jets data and applying the standard mistag matrix times a multiplicative factor. The multiplicative factor is required because the tagging rate of QCD events that enter the pretag sample is higher than the corresponding tagging rate for W + jets events.

1. The QCD fraction

The fraction of QCD events before SLTμ tagging is determined using the isolation, I (see Sec. III A), and $\not\!\!E_T$ of events with high-P_T leptons and jets. Under the assumption that I and $\not\!\!E_T$ are uncorrelated for QCD events, the number of QCD events in the $t\bar{t}$ signal region can be found by extrapolation from the nonsignal regions

$$N_D^{\mathrm{QCD}} = \frac{N_C}{N_A} N_B, \tag{8}$$

where region D, the signal region, and regions A, B, and C are defined according to

$$\text{region A: } \not\!\!E_T < 20 \text{ GeV}; \quad I > 0.2,$$
$$\text{region B: } \not\!\!E_T < 20 \text{ GeV}; \quad I < 0.1,$$
$$\text{region C: } \not\!\!E_T > 30 \text{ GeV}; \quad I > 0.2,$$
$$\text{region D: } \not\!\!E_T > 30 \text{ GeV}; \quad I < 0.1.$$

The event counts used in Eq. (8) are corrected for Monte Carlo predictions of the number of W + jets and $t\bar{t}$ events in regions A, B, and C. The QCD fraction F_{QCD} is then given by N_D^{QCD} divided by the total number of events in region D. The QCD fractions are given in Table IX.

To evaluate the accuracy of the $\not\!\!E_T$-I prediction, two complementary regions in the plane are defined as

$$\text{region E: } \not\!\!E_T < 20 \text{ GeV}; \quad 0.1 < I < 0.2,$$
$$\text{region F: } \not\!\!E_T > 30 \text{ GeV}; \quad 0.1 < I < 0.2.$$

The different regions in the $\not\!\!E_T$-I plane are shown in Fig. 9. Region F is outside the signal region and, once contamination from W + jets and $t\bar{t}$ is removed, should have a

TABLE IX. The fractions, F_{QCD}, of lepton-plus-jets events due to QCD multijet processes before SLTμ tagging. The uncertainties on the F_{QCD} values are statistical only. Also shown is the measured QCD fraction in region F, used to assign a systematic uncertainty on the F_{QCD} prediction.

	1 jet	2 jets	3 jets	≥ 4 jets	≥ 3 jets
			Electron channel		
F_{QCD}	0.0423 ± 0.0009	0.070 ± 0.002	0.049 ± 0.003	0.056 ± 0.006	0.051 ± 0.003
Region F	0.95 ± 0.04	0.97 ± 0.06	0.84 ± 0.10	1.06 ± 0.24	0.89 ± 0.09
			Muon channel		
F_{QCD}	0.0118 ± 0.0004	0.020 ± 0.001	0.013 ± 0.004	0.007 ± 0.004	0.011 ± 0.003
Region F	0.58 ± 0.05	0.65 ± 0.07	0.31 ± 0.09	2.27 ± 4.25	0.45 ± 0.13

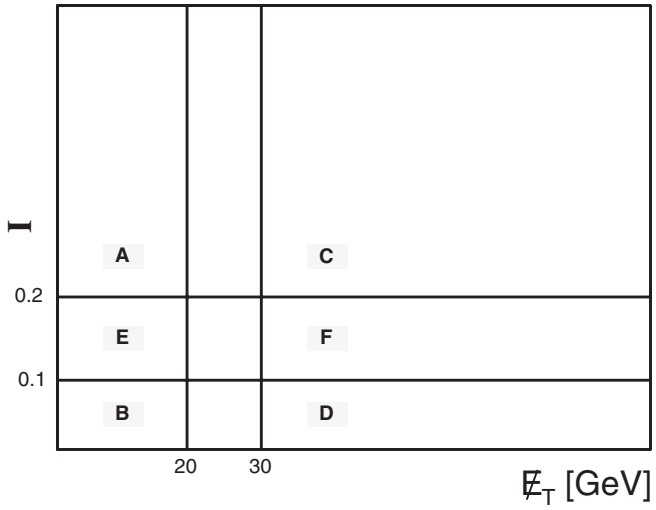

FIG. 9. A diagram illustrating the regions defined in the $\not\!\!E_T$ vs I plane.

QCD fraction, $F^F_{\rm QCD}$, of approximately 1.0. $F^F_{\rm QCD}$ is given by

$$F^F_{\rm QCD} = \frac{N_C \cdot N_E}{N_A \cdot N_F}. \quad (9)$$

We use the difference of $F^F_{\rm QCD}$ from 1.0 to estimate a systematic uncertainty on the $\not\!\!E_T$ vs I technique. The results are given in Table IX. Given the deviation from 1.0 in the ≥ 3 jets data, we assign an 11% (120%) systematic uncertainty to $F_{\rm QCD}$ for electrons (muons).

2. The tag rate of QCD events

The tag rate in QCD events that populate our signal region is enhanced relative to the rate predicted by the mistag matrix. There are two sources for this enhancement. First, much of the $\not\!\!E_T$ in QCD events is due to mismeasurement of jet energies, which is correlated with the tag rate (see Sec. VIII B). As seen in Fig. 10, the ratio of observed to predicted tags increases with $\not\!\!E_T$. Second, QCD includes $b\bar{b}$ and $c\bar{c}$ events in which the high-P_T lepton comes from the semileptonic decay of one of the b or c quarks; if the other also decays semileptonically, it may be tagged by the SLTμ.

In the $\not\!\!E_T$-I plane, the region closest kinematically to the signal region (region D) is the high-isolation and high-$\not\!\!E_T$ region, region C. Region C has the same $\not\!\!E_T$ requirement that region D does, and likewise it requires a high-P_T lepton in the event. Therefore, the tag rate measured in region C is a good representation of that of QCD events in region D.

The tag rate of QCD events is measured as an enhancement factor, k, times the W + jets mistag probability. We calculate k as the ratio of observed to predicted (by the mistag matrix) SLTμ tags in region C. The results are shown in Table X.

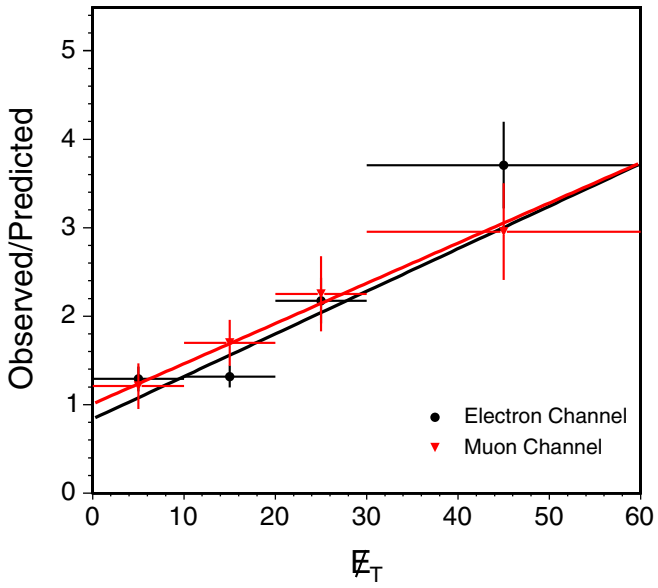

FIG. 10 (color online). The ratio of observed to predicted tags as a function of $\not\!\!E_T$ in data with a nonisolated primary lepton ($I \geq 0.2$).

3. The QCD background estimate

Having determined $F_{\rm QCD}$ and k, the QCD background is given by

$$N_{\rm QCD} = N^{W\,j{\rm tag}}_{\rm raw} \cdot k \cdot F_{\rm QCD} \quad (10)$$

where $N^{W\,j{\rm tag}}_{\rm raw}$ comes from Eq. (5).

D. Drell-Yan $\rightarrow \mu\mu$

Drell-Yan $\rightarrow \mu\mu$ events can survive the Z, Υ, and J/ψ vetoes if one muon leg fails the isolation requirement. We evaluate the number of residual Drell-Yan events that remain in the signal sample after the dimuon vetoes by measuring the number of $Z \rightarrow \mu\mu$ events in the data, $N^Z_{\rm tag}$, inside the Z mass window, where one leg of the Z is identified as an SLTμ (these events are normally removed from the signal sample). We then use an ALPGEN $Z/\gamma^* \rightarrow \mu\mu$ Monte Carlo sample to estimate the ratio, $R^{\rm out/in}$, of events outside the Z mass window to events inside. To increase the statistical precision the ratio is measured with the $\not\!\!E_T$ and H_T and dilepton rejection cuts removed and without requiring that the SLTμ be inside a jet. We use the Monte Carlo sample to measure the ratio of efficiencies $\epsilon^{\rm out}/\epsilon^{\rm in}$ of these requirements. With these pieces, the number of residual Drell-Yan events, $N_{\rm DY}$ is

$$N_{\rm DY} = N^Z_{\rm tag} \cdot R^{\rm out/in} \cdot \frac{\epsilon^{\rm out}(\not\!\!E_T, H_T, \text{dilep, SLT jet})}{\epsilon^{\rm in}(\not\!\!E_T, H_T, \text{dilep, SLT jet})}. \quad (11)$$

The results of the Drell-Yan calculation are given in Table XI.

TABLE X. Summary of the QCD background estimate. The uncertainties on the QCD fractions, F_{QCD}, and on the number of QCD events, N_{QCD}, are systematic and statistical combined. The F_{QCD} and k values listed only in the ≥ 4 jet column apply to 3, ≥ 4, and ≥ 3 jets.

	1 jet	2 jets	3 jets	≥ 4 jets	≥ 3 jets
			Electron channel		
F_{QCD}	0.042 ± 0.005	0.070 ± 0.008		0.051 ± 0.006	
k	5.3 ± 0.4	3.9 ± 0.4		3.7 ± 0.5	
N_{QCD}	82.6 ± 11.9	38.1 ± 6.1	6.3 ± 1.2	3.6 ± 0.7	9.9 ± 1.9
			Muon channel		
F_{QCD}	0.0118 ± 0.0004	0.0205 ± 0.0009		0.011 ± 0.014	
k	2.9 ± 0.4	3.4 ± 0.4		3.0 ± 0.5	
N_{QCD}	9.3 ± 11.3	6.8 ± 8.3	0.7 ± 0.9	0.4 ± 0.6	1.2 ± 1.4
			Combined channels		
Total N_{QCD}	92 ± 17	44.9 ± 10.4	7.0 ± 1.5	4.1 ± 0.9	11.1 ± 2.4

TABLE XI. Drell-Yan background summary. Uncertainties are statistical only. The values listed only in the ≥ 4 jet column apply to 3, ≥ 4, and ≥ 3 jets.

	1 jet	2 jets	3 jets	≥ 4 jets	≥ 3 jets
N^Z_{tag} (data)	27	25	3	0	3
$R^{\mathrm{out/in}}$	0.325 ± 0.003	0.315 ± 0.005		0.312 ± 0.006	
ϵ^{out} (%)	0.71 ± 0.04	1.62 ± 0.10		2.85 ± 0.24	
ϵ^{in} (%)	1.03 ± 0.05	3.10 ± 0.12		3.24 ± 0.18	
$R^{\mathrm{out/in}} \cdot \frac{\epsilon^{\mathrm{out}}}{\epsilon^{\mathrm{in}}}$	0.223 ± 0.018	0.165 ± 0.013		0.274 ± 0.027	
Drell-Yan total	6.02 ± 1.25	4.12 ± 0.88	0.82 ± 0.44	0.00 ± 0.19	0.82 ± 0.48

E. Monte Carlo driven backgrounds

Backgrounds from dibosons (WW, WZ, ZZ), $Z \rightarrow \tau^+\tau^-$, and single top are determined from Monte Carlo samples. For each of these backgrounds, the estimated number of tags is calculated as

$$N_i = \sigma_i \cdot A_i \cdot \epsilon_i \cdot \int L dt. \tag{12}$$

Here σ_i is the theoretical cross section. The acceptance, A_i, and the SLTμ tagging efficiency, ϵ_i, are calculated from the Monte Carlo samples. As with the W + HF evaluation in Sec. VII B, the efficiency includes only that due to tagging a muon from a semileptonic heavy-flavor decay. We do not include mistags in the efficiency evaluation because this is included as part of the background determined by the mistag matrix. The background evaluations are shown in Table XII.

VIII. SYSTEMATIC UNCERTAINTIES

Systematic uncertainties in this analysis come from Monte Carlo modeling of the geometrical and kinematic acceptance, knowledge of the SLTμ tagging efficiency, the effect on the acceptance of the uncertainty on the jet energy scale, uncertainties on the background predictions, and the uncertainty on the luminosity. The evaluation of the size of each of these uncertainties is described next.

A. Systematic uncertainties on acceptance and efficiency

Monte Carlo modeling of geometrical and kinematic acceptance includes effects of parton distribution functions (PDFs), initial-state radiation (ISR), final-state radiation (FSR), and jet energy scale. These are estimated by comparing different choices for PDFs, varying ISR, FSR, and the jet energy scale in the Monte Carlo model and comparing the PYTHIA generator with HERWIG.

The PDF uncertainty is evaluated from 3 contributions. The first is obtained by varying the PDF according to 20 eigenvectors [10] that account for the uncertainty on the PDF fit. The second is the difference between the CTEQ5L PDF used for the acceptance measurement with that obtained using MRST98 [21] in the default configuration to account for the type of PDF fit used. The third is evaluated comparing the default MRST with two alternative choices of α_s to get an estimate of the uncertainty due to the value of α_s. The three contributions in quadrature yield an acceptance uncertainty of 0.9%. We note that there are more modern CTEQ PDF sets [22] that might reduce this uncertainty.

The uncertainty due to the limited knowledge of ISR is constrained by studies of radiation in Drell-Yan events in the data. We vary both ISR and FSR in the $t\bar{t}$ Monte Carlo model within the allowed range and add the deviations in quadrature. The systematic uncertainty due to this effect is 0.8%.

The uncertainty on the acceptance due to the uncertainty in the jet energy scale is measured by shifting the energies of the jets in the $t\bar{t}$ Monte Carlo model by $\pm 1\sigma$ of the jet energy scale [23]. The resulting uncertainty on the acceptance is 4.1%.

The effects of generator modeling of the $t\bar{t}$ kinematics are measured by comparing the acceptance from PYTHIA and HERWIG. The result is a 2.4% uncertainty.

As described in Sec. VA, a scale factor is applied to the $t\bar{t}$ Monte Carlo data set to correct for lepton identification (ID) efficiency differences between data and Monte Carlo events. This scale factor has an associated uncertainty that yields a 2.9% uncertainty on the total $t\bar{t}$ acceptance.

The systematic uncertainty on the SLTμ tagging efficiency in $t\bar{t}$ events is comprised of three parts: first, the uncertainty due to the P_T dependence of the SLTμ efficiency curves which is evaluated by remeasuring the $t\bar{t}$ event tagging efficiency with the $\pm 1\sigma$ curves shown as the dashed lines in Figs. 3 and 4. Next, the tagging efficiency measurement assumes that the efficiency for finding tracks in jets in the COT is properly modeled in the simulation. This assumption comes with a 5% uncertainty, which was evaluated by embedding Monte Carlo tracks in data events. Finally, the statistical uncertainty on the SLTμ efficiency in $t\bar{t}$ events is absorbed as a systematic uncertainty. The three contributions combine to give a systematic uncertainty of 5.1%.

TABLE XII. Summary of Monte Carlo derived backgrounds. The theoretical cross sections [18–20] are inclusive. The acceptance, A, includes the branching fraction to events with N jets, and the efficiency for finding an SLTμ in these events is ϵ.

	1 jet	2 jet	3 jets	≥ 4 jets	≥ 3 jets
			WW		
σ_{theory}			12.4 ± 1.2 pb		
A (%)	2.44 ± 0.01	2.62 ± 0.01	0.403 ± 0.004	0.121 ± 0.002	0.524 ± 0.005
ϵ (%)	0.49 ± 0.03	0.76 ± 0.04	0.88 ± 0.09	1.56 ± 0.23	1.06 ± 0.09
N_{WW}	2.986 ± 0.299	5.001 ± 0.394	0.892 ± 0.190	0.475 ± 0.118	1.395 ± 0.228
			WZ		
σ_{theory}			3.96 ± 0.40 pb		
A (%)	1.085 ± 0.007	1.317 ± 0.007	0.233 ± 0.003	0.070 ± 0.002	0.302 ± 0.004
ϵ (%)	0.85 ± 0.06	1.72 ± 0.07	1.46 ± 0.16	2.69 ± 0.39	1.77 ± 0.15
N_{WZ}	0.740 ± 0.075	1.821 ± 0.128	0.274 ± 0.044	0.151 ± 0.036	0.432 ± 0.058
			ZZ		
σ_{theory}			3.4 ± 0.3 pb		
A (%)	0.104 ± 0.002	0.097 ± 0.002	0.060 ± 0.001	0.012 ± 0.001	0.042 ± 0.001
ϵ (%)	1.0 ± 0.2	2.4 ± 0.3	2.3 ± 0.5	1.6 ± 0.5	2.1 ± 0.4
N_{ZZ}	0.07 ± 0.02	0.16 ± 0.05	0.05 ± 0.02	0.013 ± 0.006	0.06 ± 0.02
			Drell-Yan $\rightarrow \tau\tau$		
σ_{theory}			333 ± 4.2 pb		
A (%)	0.112 ± 0.001	0.054 ± 0.001	0.0058 ± 0.0004	0.0014 ± 0.0002	0.0073 ± 0.0004
ϵ (%)	0.4 ± 0.1	0.4 ± 0.1	1.6 ± 0.7	1.3 ± 0.5	1.3 ± 0.5
$N_{\text{Drell-Yan}\rightarrow\tau\tau}$	2.65 ± 0.57	1.54 ± 0.43	0.65 ± 0.28	0.13 ± 0.05	0.65 ± 0.27
			s-channel single top		
σ_{theory}			0.88 ± 0.11 pb		
A (%)	1.12 ± 0.01	2.66 ± 0.01	0.717 ± 0.005	0.203 ± 0.003	0.920 ± 0.006
ϵ (%)	5.0 ± 0.1	9.7 ± 0.1	10.2 ± 0.2	11.1 ± 0.4	10.4 ± 0.2
$N_{s\text{ chan}}$	1.00 ± 0.11	4.61 ± 0.46	1.31 ± 0.15	0.40 ± 0.05	1.71 ± 0.19
			t-channel single top		
σ_{theory}			1.98 ± 0.08 pb		
A (%)	1.91 ± 0.01	2.10 ± 0.01	0.345 ± 0.003	0.057 ± 0.001	0.402 ± 0.004
ϵ (%)	4.38 ± 0.09	5.19 ± 0.09	5.96 ± 0.24	7.37 ± 0.64	6.16 ± 0.22
$N_{t\text{ chan}}$	3.36 ± 0.37	4.39 ± 0.47	0.83 ± 0.11	0.17 ± 0.03	1.00 ± 0.13

Adding all these contributions in quadrature gives a total ''acceptance modeling and efficiency'' systematic uncertainty of 7.7%.

B. Systematic uncertainty of the mistag prediction

To measure the uncertainty on the predicted number of tags in light-flavor jets, we test the predictive power of the mistag matrix on large samples of events triggered on a single jet with an (uncorrected) E_T threshold of 20, 50, 70, or 100 GeV. Care must be taken in several areas. Because of the E_T threshold on one jet in the event, that ''trigger jet'' will have a bias against SLTμ tags because particles that reach the muon chambers do not deposit all their energy in the calorimeter and therefore reduce the measured jet energy from its true value. Therefore, if no other jet is above the trigger threshold, we remove the trigger jet from the sample used to test the mistag prediction. If there is an additional jet above the trigger threshold, then all jets above threshold are used. The opposite effect occurs in jets that are measured well below trigger threshold. In a dijet event triggered, for instance, with a 100 GeV threshold, a single recoil jet with energy well below 100 GeV is likely to be significantly mismeasured. Such jets have an enhanced rate of SLTμ tags relative to jets in W + jets events because jet mismeasurement is correlated with the population of SLTμ tags through detector cracks, hadronic punchthrough of the calorimeter, and real muon content. In addition to rejecting the trigger jet, we reject jets in dijet events if the recoil jet falls below the trigger threshold. For events with higher jet multiplicities we use only tracks in jets that are separated from the trigger-jet axis by ΔR between 0.7 and 2.6. These various criteria have been chosen in order to provide, in the jet samples, a set of jets that are similar in terms of SLTμ tags to those found in W + jets events [5].

To increase the number of jets available for the study we use, in addition to the jet triggered data, events triggered on a single photon candidate (γ + jets) with a threshold of 25, 50, or 70 GeV, and a ΣE_T-triggered sample, triggered on a four-jet total energy of at least 100 GeV. Jets in the γ + jets events are selected in the same way as in the single jet triggered events. All jets above 20 GeV are used in the ΣE_T sample.

Since the mistag matrix is designed to predict the number of tags from light-flavor jets, we must also suppress heavy-flavor jets in our sample. This is achieved by removing events in which any jet has an identified secondary vertex [3], or in which the mass of the tracks contained in a potential secondary vertex is greater than 0.3 GeV/c^2, or in which any jet contains a track with an impact parameter significance $(d_0/\sigma_{d_0}) \geq 2$. This is found [5] to provide sufficient suppression of heavy-flavor jets while leaving the remaining sample unbiased against decays in flight inside the jet.

With the above jet selection, the systematic uncertainty is determined using the difference between the number of SLTμ tags predicted by the mistag matrix and those observed in the data. The results are shown, as a function of the E_T of the jet in Table XIII.

TABLE XIII. Checks of the mistag matrix in different jet E_T bins. Δ = (Pred-Obs)/Pred. These values of Δ are weighted using the W + 3-or-more jets distribution to determine a systematic uncertainty on the mistag prediction.

Jet E_T^{corr} (GeV)	Observed	Predicted	Δ (%)
20–30	1892	1641 ± 29	−15.3 ± 3.3
30–45	1561	1693 ± 45	7.8 ± 3.4
45–65	701	768 ± 46	8.7 ± 6.4
65–90	464	462 ± 46	−0.5 ± 11.0
≥ 90	466	466 ± 76	−0.1 ± 16.9
≥ 20	5084	5029 ± 219	−1.1 ± 4.6

Finally, we use the E_T spectrum of W + jets events from the Monte Carlo sample to perform a weighted average over the deviations between predicted and observed tags given in Table XIII. The result is (predicted SLTμ–observed SLTμ)/pred = (0.1 ± 4.4)%. We assign a systematic uncertainty of 5% on the prediction of the mistag matrix.

C. Other background uncertainties

1. W + heavy-flavor uncertainties

Three sources contribute to the uncertainty on the $Wb\bar{b} + Wc\bar{c} + Wc$ background prediction: the choice of ALPGEN settings, the uncertainty associated with the scaling factor that takes the heavy-flavor fraction in ALPGEN to the data, and the uncertainty on the tagging efficiency. The determination of the uncertainties on the ALPGEN settings and the scale factor are described in Sec. VII B. The ALPGEN settings contribute 23% to the W + heavy-flavor background uncertainty and the scale factor another 30%. The uncertainty on the heavy-flavor tagging efficiency is the same as that for the $t\bar{t}$ tagging efficiency described in Sec. VIII A. The correlation between the efficiency for the background determination and for the $t\bar{t}$ acceptance is taken into account.

2. QCD background uncertainties

Uncertainties on the QCD background prediction are determined using the level of agreement between predicted and measured events in region F, as described in Sec. VII C 1. We assign a systematic uncertainty on the F_{QCD} measurement of 11% for electrons and 120% for muons, given conservatively by the worst agreement of the region F prediction in each case. We fold this in with the statistical uncertainty on the F_{QCD} determination, the uncertainty on the correction factor k, both given in Table X, and the 5% systematic uncertainty due to the application of the mistag matrix. The total QCD background uncertainty is 19% and 124% for electrons and muons, respectively. In

TABLE XIV. Summary of systematic uncertainties.

Source	Fractional sys. uncert. (%)	$\Delta\sigma_{t\bar{t}}$ (%)
Acceptance modeling and SLT tagging efficiency	7.7	+8.3 −7.5
Mistag matrix prediction	5	3.6
$Wb\bar{b} + Wc\bar{c} + Wc$ prediction	38	5.3
QCD prediction	19 (e) 124 (μ)	1.1
Drell-Yan and other MC backgrounds	11	0.4
Total systematic uncertainty		+10.5 −10.0

the final determination of the QCD systematic, we add in quadrature the separate effects on the cross section of the QCD uncertainties for electrons and muons. The estimate of the QCD background is correlated with the estimates of the mistags and W + heavy-flavor backgrounds [Eqs. (6), (7), and (10)]. This is taken into account when determining the effect on the $t\bar{t}$ cross section. Together with a relatively small QCD fraction of the events, the result is a rather small effect on the cross section determination, despite the large uncertainty on the QCD fraction itself.

3. Other background uncertainties

The systematic uncertainty on the small Drell-Yan background is determined by the statistical uncertainty of the estimate. Uncertainties on the Monte Carlo background predictions come from uncertainties in the cross sections for the various processes and from the event sizes of the Monte Carlo samples. This uncertainty is reflected in the uncertainties quoted in Sec. VII E. The combined uncertainty on the Drell-Yan and Monte Carlo-derived backgrounds is 11%.

D. Summary of systematic uncertainties

The systematic uncertainties are summarized in Table XIV. An additional systematic due to the uncertainty on the luminosity determination (5.9% [7]) is treated separately.

IX. $t\bar{t}$ PRODUCTION CROSS SECTION

Before calculating the cross section, the estimated number of background events is corrected for $t\bar{t}$ events in the pretag sample using a simple iterative procedure. This is required because we apply the mistag matrix to the events before tagging to estimate the mistag and QCD backgrounds and also use the pretag sample in the W + heavy-flavor background determination assuming no $t\bar{t}$ content. A summary of the number of observed events and the background predictions, both before and after the correction, as a function of the number of jets is given in Table XV. It is worth noting the excellent agreement between the expected and observed tagged events in the W + 1 and 2 jet samples, where the expectation is dominated by the mistag contribution, and the $t\bar{t}$ contribution is negligible. This is a further validation of the mistag matrix.

The cross section is calculated as

$$\sigma_{t\bar{t}} = \frac{N_{\rm obs} - N_{\rm bkg}}{A_{t\bar{t}} \cdot \epsilon_{t\bar{t}} \cdot \int L dt}, \tag{13}$$

where $N_{\rm obs}$ is the number of events with ≥ 3 jets in which at least one jet has an SLTμ tag, $N_{\rm bkg}$ is the corrected background, $A_{t\bar{t}}$ and $\epsilon_{t\bar{t}}$ are the $t\bar{t}$ event acceptance and

TABLE XV. Number of tagged events and the background summary. The uncertainty on the total background is not a simple sum in quadrature of the individual backgrounds because of the correlation between the mistag, W + heavy-flavor, and QCD background predictions.

	$H_T \geq 0$ GeV		$H_T \geq 200$ GeV		
Background	1 jet	2 jet	3 jets	≥ 4 jets	≥ 3 jets
Taggable events	75 595	18 264	2587	1120	3707
Mistags	622 ± 31	226 ± 12	53.0 ± 2.7	31.4 ± 1.6	84.5 ± 4.3
$Wb\bar{b} + Wc\bar{c} + Wc$	145 ± 55	66.6 ± 25.2	15.3 ± 5.8	8.5 ± 3.2	23.0 ± 8.7
QCD multijet	91.9 ± 16.5	44.9 ± 10.4	7.0 ± 1.5	4.1 ± 0.9	11.1 ± 2.4
$WW + WZ + ZZ$	3.80 ± 0.44	6.98 ± 0.66	1.21 ± 0.23	0.64 ± 0.14	1.88 ± 0.30
Drell-Yan $\rightarrow \tau^+\tau^-$	2.65 ± 0.57	1.54 ± 0.43	0.65 ± 0.28	0.13 ± 0.05	0.65 ± 0.27
Drell-Yan $\rightarrow \mu^+\mu^-$	6.02 ± 1.25	4.12 ± 0.88	0.82 ± 0.44	0.00 ± 0.19	0.82 ± 0.48
Single top	4.36 ± 0.39	9.00 ± 0.66	2.14 ± 0.18	0.57 ± 0.06	2.71 ± 0.23
Total background	876.5 ± 53.6	359.0 ± 24.0	80.2 ± 5.4	45.3 ± 3.0	124.6 ± 8.2
Corrected background	...	...	79.5 ± 5.3		79.5 ± 5.3
$t\bar{t}$ expectation ($\sigma = 6.70$)	2.60 ± 0.33	23.5 ± 1.8	50.1 ± 3.6	74.2 ± 6.5	124.3 ± 9.1
Total background + $t\bar{t}$	879.1 ± 53.6	382.5 ± 24.1	203.9 ± 10.6		203.9 ± 10.6
Tagged events	892	384	142	106	248

TABLE XVI. Summary of components of the denominator for the cross section calculation. The $t\bar{t}$ acceptance and tagging efficiency for 3-or-more-jets events is determined using the PYTHIA Monte Carlo simulation.

	Electrons	CMUP muons	CMX muons
Acc. no tag (%)	$3.71 \pm 0.01 \pm 0.21$	$2.05 \pm 0.01 \pm 0.14$	$0.946 \pm 0.004 \pm 0.050$
Event tagging eff. (%)	$14.02 \pm 0.08 \pm 0.72$	$13.07 \pm 0.10 \pm 0.67$	$13.38 \pm 0.16 \pm 0.68$
Acc. with tag (%)	$0.520 \pm 0.003 \pm 0.039$	$0.268 \pm 0.002 \pm 0.022$	$0.127 \pm 0.002 \pm 0.009$
Luminosity (pb^{-1})	2033.6 ± 119.6	2033.6 ± 119.6	1992.5 ± 117.2
Denominator (pb^{-1})	$10.58 \pm 0.07 \pm 0.80 \pm 0.62$	$7.97 \pm 0.06 \pm 0.49 \pm 0.47$	
Total denominator (pb^{-1})	$18.56 \pm 0.09(\text{stat}) \pm 0.94(\text{sys}) \pm 1.09(\text{lum})$		

tagging efficiency, and $\int Ldt$ is the integrated luminosity. The acceptance and efficiency are discussed in Sec. V, and summarized for the signal region in Table XVI. We measure a total $t\bar{t}$ cross section of

$$\sigma(p\bar{p} \to t\bar{t}X) = 9.1 \pm 1.1^{+1.0}_{-0.9} \pm 0.6 \text{ pb}, \qquad (14)$$

where the first uncertainty is statistical, the second is systematic, and the third is from the luminosity. This cross section value uses acceptances and tagging efficiencies appropriate for a top mass of 175 GeV/c^2. The acceptances and efficiencies, and therefore the calculated cross section, change slightly for other assumed top masses. The calculated cross section is 3% higher assuming a top mass of 170 GeV/c^2, and 4% lower assuming a top mass of 180 GeV/c^2. As a check we also measure the cross section separately for events in which the primary lepton is an electron and in which it is a muon. We measure 9.5 ± 1.2 pb when the primary lepton is an electron and 8.5 ± 1.2 pb when it is a muon. The uncertainties in both cases are statistical only.

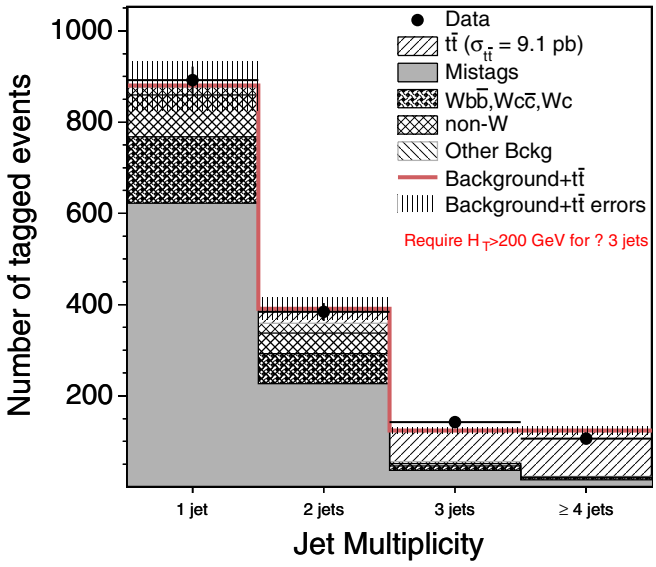

FIG. 11 (color online). The expected background and observed tags in W + 1, 2, 3, and 4-or-more jets events. The expected $t\bar{t}$ contribution is normalized to the measured cross section.

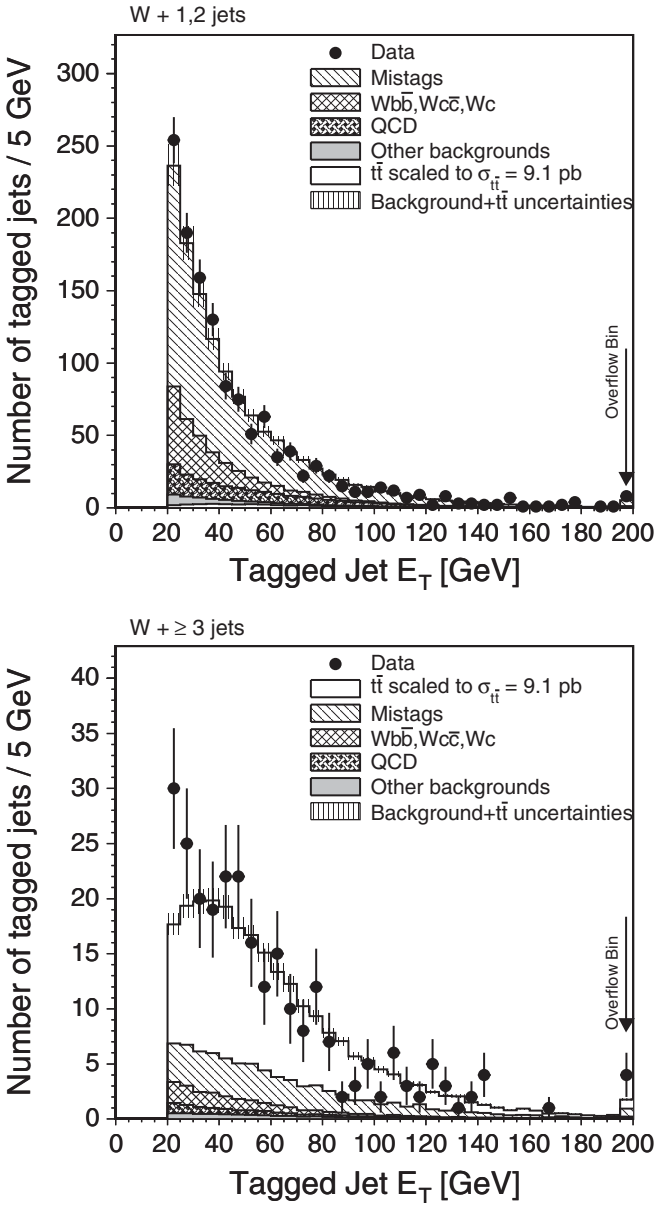

FIG. 12. Comparison of the jet E_T distributions for tagged jets and for expectations from mistags, W + heavy-flavor, QCD and $t\bar{t}$ events. The upper plot is for W + 1- and 2-jet events and the lower plot for W + 3-or-more-jets events.

Figure 11 shows, in bins of the number of jets in W + jets candidates, the expected number of tagged background and $t\bar{t}$ (normalized to the measured cross section) events together with the number of observed SLTμ tags.

In Figs. 12–14 we examine a few kinematic features of the tagged events. In each case the data are compared to the expected backgrounds plus $t\bar{t}$, normalized to the measured cross section. The agreement between data and expectation is good. The only slight exceptions are a few bins at low E_T in the $W+ \geq 3$ jet events in Fig. 12, where the number of observed tags exceeds somewhat the expectation. This is consistent with the excess seen in the low E_T jet data in

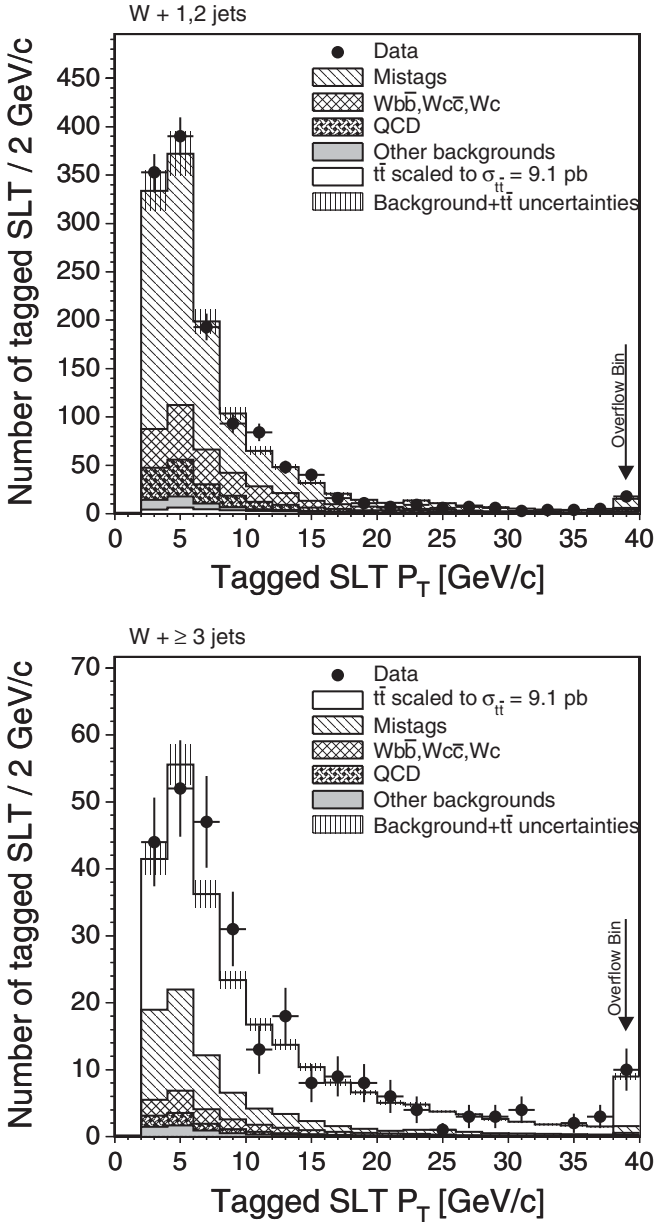

FIG. 13. P_T of the SLTμ tags compared with expectations from backgrounds and $t\bar{t}$. The upper plot is for W + 1- and 2-jet events and the lower plot for $W+ \geq 3$-jet events.

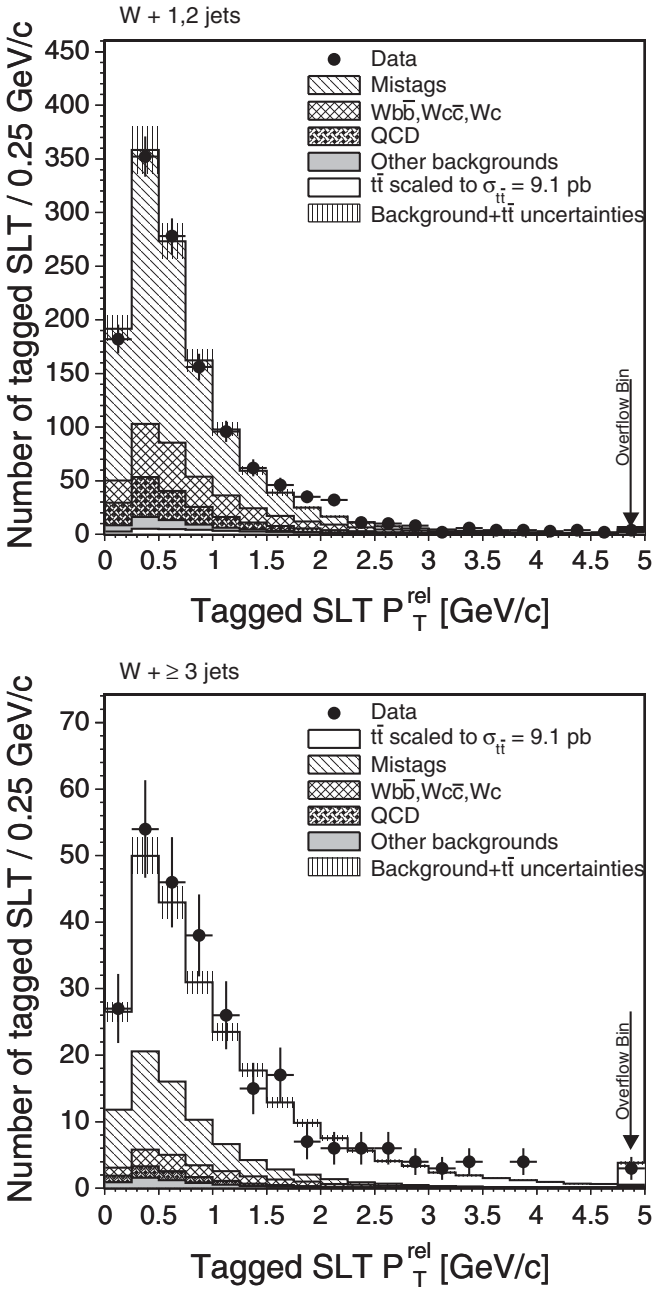

FIG. 14. The distribution of P_T relative to the jet axis (P_T^{rel}) for tags in data, compared with expectations from backgrounds plus $t\bar{t}$. The upper plot is for 1- and 2-jet events and the lower plot for $\geq$ 3-jet events.

Table XIII, which is folded into the systematic uncertainty on the measurement.

X. CONCLUSIONS

Using 2 fb^{-1} of integrated luminosity collected by the CDF II detector, we have measured the total cross section for $t\bar{t}$ production in $p\bar{p}$ collisions with a center-of-mass energy, $\sqrt{s} = 1.96$ TeV. The measurement begins by selecting a data set of W + jets candidates. We separate

signal from background by identifying candidate semileptonic decays of b-hadrons into muons. This technique was first published in Ref. [4]. This measurement is an update that uses 10 times the amount of data of the previous measurement and a new technique for evaluating the dominant background (see Sec. VI) of misidentifying a jet from a light-flavor quark as one containing a b-hadron. The measured $t\bar{t}$ cross section is

$$\sigma(p\bar{p} \rightarrow t\bar{t}X) = 9.1 \pm 1.1^{+1.0}_{-0.9} \pm 0.6 \text{ pb}, \qquad (15)$$

consistent with the expectation of $6.7^{+0.7}_{-0.9}$ pb for standard model production and decay of top quark pairs with a mass of 175 GeV$/c^2$. The measurement agrees well with other CDF measurements of the $t\bar{t}$ production cross section [24], as well as with the most recent publications from D0 [25]. Assuming the cross section increases 0.2 pb for every 1 GeV$/c^2$ decrease in the top mass, then at the world average top mass of 172.4 GeV$/c^2$ the theoretical cross section is approximately 7.2 pb. Using a linear fit to the mass dependence, the measured cross section was estimated at the world average top mass and is found to be 8.9 ± 1.6 pb. The kinematic distributions of the tagged sample are also consistent with standard model expectations. The observed number of tags in $W + 1$- and 2-jet events is in excellent agreement with expectations from background, indicating that the backgrounds are well understood.

ACKNOWLEDGMENTS

We thank the Fermilab staff and the technical staffs of the participating institutions for their vital contributions. This work was supported by the U.S. Department of Energy and the National Science Foundation; the Italian Istituto Nazionale di Fisica Nucleare; the Ministry of Education, Culture, Sports, Science and Technology of Japan; the Natural Sciences and Engineering Research Council of Canada; the National Science Council of the Republic of China; the Swiss National Science Foundation; the A. P. Sloan Foundation; the Bundesministerium für Bildung und Forschung, Germany; the Korean Science and Engineering Foundation and the Korean Research Foundation; the Science and Technology Facilities Council and the Royal Society, UK; the Institut National de Physique Nucleaire et Physique des Particules/CNRS; the Russian Foundation for Basic Research; the Ministerio de Ciencia e Innovación, and the Programa Consolider-Ingenio 2010, Spain; the Slovak R&D Agency; and the Academy of Finland.

[1] M. Cacciari *et al.*, J. High Energy Phys. 09 (2008) 127; N. Kidonakis and R. Vogt, Phys. Rev. D **78**, 074005 (2008); S. Moch and P. Uwer, Nucl. Phys. B, Proc. Suppl. **183**, 75 (2008).

[2] We use a (z, ϕ, θ) coordinate system where the z-axis is in the direction of the proton beam, and ϕ and θ are the azimuthal and polar angles, respectively. The pseudorapidity, η, is defined as $-\ln(\tan\frac{\theta}{2})$. The transverse momentum of a charged particle is $P_T = P\sin\theta$, where P represents the measured momentum of the charged-particle track. The analogous quantity using calorimeter energies, defined as $E_T = E\sin\theta$, is called transverse energy. The missing transverse energy is defined as $\not\!\!E_T = -|\sum_i E^i_T \hat{n}_i|$ where E^i_T is the magnitude of the transverse energy contained in each calorimeter tower i in the pseudorapidity region $|\eta| < 3.6$ and $\hat{n}_i$ is the direction unit vector of the tower in the plane transverse to the beam direction.

[3] A. Abulencia *et al.* (CDF Collaboration), Phys. Rev. Lett. **97**, 082004 (2006); D. Acosta *et al.* (CDF Collaboration), Phys. Rev. D **71**, 052003 (2005).

[4] D. Acosta *et al.* (CDF Collaboration), Phys. Rev. D **72**, 032002 (2005).

[5] Ulysses Allen Grundler, Ph.D. thesis, University of Illinois at Urbana-Champaign, Urbana, IL, 2008, FERMILAB-THESIS-2008-27.

[6] The CDF II Detector Technical Design Report No. Fermilab-Pub-96/390-E; D. Acosta *et al.*, Phys. Rev. D **71**, 052003 (2005).

[7] S. Klimenko, J. Konigsberg, and T. M. Liss, Fermilab Report No. Fermilab-FN-0741.

[8] T. Sjostrand *et al.*, Comput. Phys. Commun. **135**, 238 (2001).

[9] G. Corcella *et al.*, J. High Energy Phys. 01 (2001) 10.

[10] H. L. Lai *et al.*, Eur. Phys. J. C **12**, 375 (2000).

[11] D. J. Lange *et al.*, Nucl. Instrum. Methods Phys. Res., Sect. A **462**, 152 (2001).

[12] M. Mangano *et al.*, J. High Energy Phys. 07 (2003) 1.

[13] Daniel Sherman, Ph.D. thesis, Harvard University.

[14] F. Maltoni and T. Stelzer, J. High Energy Phys. 02 (2003) 27.

[15] E. Gerchtein and M. Paulini, ECONF C0303241, TUMT005 (2003), arXiv:physics/0306031.

[16] D. Acosta *et al.* (CDF Collaboration), Phys. Rev. Lett. **91**, 241804 (2003); A. Abulencia *et al.* (CDF Collaboration), Phys. Rev. D **74**, 031109 (2006).

[17] A. Abulencia *et al.* (CDF Collaboration), Phys. Rev. Lett. **98**, 122001 (2007).

[18] J. M. Campbell and R. K. Ellis, Phys. Rev. D **60**, 113006 (1999). The ZZ cross section of 3.4 pb is appropriate for the PYTHIA Monte Carlo sample we use that includes events with one off-shell Z. The value is arrived at by

normalizing the PYTHIA sample to the Campbell and Ellis cross section of 1.58 pb for two on-shell Z bosons.

[19] D. Acosta *et al.* (CDF Collaboration), Phys. Rev. Lett. **94**, 091803 (2005).

[20] Z. Sullivan, Phys. Rev. D **70**, 114012 (2004).

[21] A. D. Martin, R. G. Roberts, W. J. Stirling, and R. S. Thorne, Eur. Phys. J. C **4**, 463 (1998).

[22] J. Pumplin *et al.*, J. High Energy Phys. 07 (2002) 012.

[23] A. Bhatti *et al.*, Nucl. Instrum. Methods Phys. Res., Sect. A **566**, 375 (2006).

[24] The CDF Collaboration, CDF Conference note 9448 (2008), http://www-cdf.fnal.gov/physics/new/top/confNotes/.

[25] V. M. Abazov *et al.* (D0 Collaboration), Phys. Rev. Lett. **100**, 192003 (2008); **100**, 192004 (2008).